OPEN ACCESS



The Compact Structures of Massive $z \sim 0.7$ Post-starburst Galaxies in the SQuIGGLE Sample

David J. Setton 1 , Margaret Verrico 1 , Rachel Bezanson 1 , Jenny E. Greene 2 , Katherine A. Suess 3,4 , Andy D. Goulding 2 , Justin S. Spilker 5,6,13 , Mariska Kriek 7 , Robert Feldmann 8 , Desika Narayanan , Khalil Hall-Hooper 1 , and Erin Kado-Fong 2 , and Erin Kado-Fong

Department of Physics and Astronomy and PITT PACC, University of Pittsburgh, Pittsburgh, PA 15260, USA; davidsetton@pitt.edu

Department of Astrophysical Sciences, Princeton University, Princeton, NJ 08544, USA

Department of Astronomy and Astrophysics, University of California, Santa Cruz, 1156 High Street, Santa Cruz, CA 95064, USA
 Kavli Institute for Particle Astrophysics and Cosmology and Department of Physics, Stanford University, Stanford, CA 94305, USA
 Department of Astronomy, University of Texas at Austin, 2515 Speedway, Stop C1400, Austin, TX 78712, USA

Department of Physics and Astronomy and George P. and Cynthia Woods Mitchell Institute for Fundamental Physics and Astronomy, Texas A&M University, 4242

TAMU, College Station, TX 77843-4242, USA

Leiden Observatory, Leiden University, P.O. Box 9513, NL-2300 AA Leiden, The Netherlands
 Institute for Computational Science, University of Zurich, CH-8057 Zurich, Switzerland
 Department of Astronomy, University of Florida, 211 Bryant Space Science Center, Gainesville, FL 32611, USA

University of Florida Informatics Institute, 432 Newell Drive, CISE Bldg E251, Gainesville, FL 32611, USA
 Cosmic Dawn Centre at the Niels Bohr Institue, University of Copenhagen and DTU-Space, Technical University of Denmark, Denmark Department of Mathematics, North Carolina State University, 2108 SAS Hall Box 8205, Raleigh, NC 27695, USA
 Received 2021 December 23; revised 2022 February 28; accepted 2022 March 17; published 2022 May 24

Abstract

We present structural measurements of 145 spectroscopically selected intermediate-redshift ($z \sim 0.7$), massive ($M_{\star} \sim 10^{11} \, M_{\odot}$) post-starburst galaxies from the SQuIGG \vec{L} E sample measured using wide-depth Hyper Suprime-Cam *i*-band imaging. This deep imaging allows us to probe the sizes and structures of these galaxies, which we compare to a control sample of star-forming and quiescent galaxies drawn from the LEGA-C Survey. We find that post-starburst galaxies systematically lie ~ 0.1 dex below the quiescent mass—size (half-light radius) relation, with a scatter of ~ 0.2 dex. This finding is bolstered by nonparametric measures, such as the Gini coefficient and the concentration, which also reveal these galaxies to have more compact light profiles than both quiescent and star-forming populations at similar mass and redshift. The sizes of post-starburst galaxies show either negative or no correlation with the time since quenching, such that more recently quenched galaxies are larger or similarly sized. This empirical finding disfavors the formation of post-starburst galaxies via a purely central burst of star formation that simultaneously shrinks the galaxy and shuts off star formation. We show that the central densities of post-starburst and quiescent galaxies at this epoch are very similar, in contrast with their effective radii. The structural properties of $z \sim 0.7$ post-starburst galaxies match those of quiescent galaxies that formed in the early universe, suggesting that rapid quenching in the present epoch is driven by a similar mechanism to the one at high redshift.

Unified Astronomy Thesaurus concepts: Post-starburst galaxies (2176); Galaxy quenching (2040); Galaxy evolution (594); Quenched galaxies (2016); Galaxies (573)

Supporting material: machine-readable tables

1. Introduction

Broadly speaking, galaxies in the universe can be divided into star-forming and quiescent populations. These populations of galaxies are distinct in that star-forming galaxies form many stars at a rate that is proportional to their stellar mass (e.g., Whitaker et al. 2012b), whereas quiescent galaxies form few or no stars. In addition, the two populations differ structurally at all epochs; star-forming galaxies as a population are systematically larger and less compact than the coeval quiescent population at fixed stellar mass (e.g., van der Wel et al. 2014; Mowla et al. 2019; Kawinwanichakij et al. 2021). This indicates that a structural transformation may be coincident

Original content from this work may be used under the terms of the Creative Commons Attribution 4.0 licence. Any further distribution of this work must maintain attribution to the author(s) and the title of the work, journal citation and DOI.

with the shutdown of star formation, a process that is jointly referred to as "quenching."

There is a growing body of evidence that two distinct pathways to quiescence exist: slow quenching that dominates at low redshift as galaxies gradually exhaust their gas supplies and high-redshift rapid quenching that often follows a period of significant starburst (Wu et al. 2018; Belli et al. 2019; Suess et al. 2021), though there is a significant diversity in quenching times especially among the galaxies which quench more slowly (e.g., Tacchella et al. 2022). The existence of quenched galaxies at high redshift (e.g., Straatman et al. 2014; Davidzon et al. 2017; Tanaka et al. 2019; D'Eugenio et al. 2020a; Forrest et al. 2020; Valentino et al. 2020; Kalita et al. 2021; McLeod et al. 2021) indicates that the seeds of the most massive quiescent galaxies in the local universe formed on very short timescales through this rapid mode. However, it is still unclear what causes massive galaxies to abruptly quench after an intense period of star formation, and simulations need to invoke various forms feedback to actively suppress star formation and

¹³ NHFP Hubble Fellow.

prevent the formation of over-massive galaxies (e.g., Schaye et al. 2015; Sijacki et al. 2015). As such, placing empirical constraints on the quenching process, especially in the rapid channel, is essential to understanding the precise process galaxies undergo as they shut off their final epoch of star-forming activity.

Ideally, this process could be studied by finding galaxies at the exact moment preceding the rapid shutdown of their most recent episode of star formation. Unfortunately, rapid shutdown by definition occurs on extremely fast timescales, and it is difficult to identify populations in the midst of shutdown, especially given the uncertainty of future star formation activity in any galaxy experiencing a starburst at the time of observation. However, it is instead possible to identify the immediate descendants of galaxies that went through the rapid channel by looking for galaxies whose spectra are dominated by a stellar population that formed in the last <1 Gyr but that show no evidence of recent star formation. These galaxies are often referred to as post-starburst, or "K+A" galaxies, due to their composite spectral energy distributions (SEDs), which are dominated by late-type B and A type stars (Dressler & Gunn 1983; Zabludoff & Zaritsky 1995).

Numerous methods have been developed to select poststarburst galaxies, including Balmer absorption strength in conjunction with a measure of weak nebular emission (e.g., Pracy et al. 2005; Yagi & Goto 2006; French et al. 2015; Wu et al. 2018; Chen et al. 2019), "K+A" template fitting (e.g., Pattarakijwanich et al. 2016), photometric supercolors (e.g., Wild et al. 2014; Almaini et al. 2017; Maltby et al. 2018; Wilkinson et al. 2021), or UVJ color space (e.g., Belli et al. 2019; Suess et al. 2020). All these methods have in common the goal of selecting galaxies with light dominated by a young stellar population with no ongoing star formation (for a detailed review of post-starburst selection methods, see French 2021). Although a dramatic burst of star formation is not strictly required as suggested by the term post-starburst—the spectral signatures seen in post-starburst galaxies can be produced by the truncation of the existing high star formation rate—it is thought that bursts do accompany quenching in high-mass galaxies (e.g., French et al. 2015; Wild et al. 2020; Suess et al. 2022). Post-starburst galaxies serve as a laboratory for understanding the progenitors of the rapid quenching channel and their evolution immediately after star formation shuts off can shed light on the conditions that caused the galaxies to cease forming new stars.

One important empirical probe of the quenching of massive galaxies comes from the study of their structures. Because starforming galaxies at any given epoch are consistently larger than quiescent galaxies (e.g., van der Wel et al. 2014; Mowla et al. 2019; Kawinwanichakij et al. 2021), it has been suggested that mergers can drive both the quenching and structural transformation of galaxies by driving gas inward and rendering a more compact aggregate light profile with the resulting centralized star formation (Wellons et al. 2015; Zheng et al. 2020; Pathak et al. 2021). Mergers appear to be very common in poststarburst galaxies (Zabludoff et al. 1996; Pawlik et al. 2016; Sazonova et al. 2021), and in simulations mergers have been shown to result in an enhancement in the quiescent fraction in post-merger systems (Quai et al. 2021). A number of structural studies of post-starburst populations have found that they are compact relative to both coeval star-forming and quiescent populations (Yano et al. 2016; Almaini et al. 2017; Maltby

et al. 2018; Wu et al. 2018; Suess et al. 2020) and have younger central stellar populations than their outskirts (Chen et al. 2019; D'Eugenio et al. 2020b; Wu 2021). However, the evidence for the ubiquity of merger-driven central starbursts as the driver of structural transformation is inconclusive. The most massive post-starburst galaxies at intermediate-to-high redshift have been found to lack color or age gradients (Maltby et al. 2018; Setton et al. 2020; Suess et al. 2020), disfavoring out purely nuclear starbursts and implying that star formation prior to quenching may have occurred on kiloparsec scales. These field studies are in contrast with observations of post-starburst galaxies in dense clusters, where environmental effects such as ram pressure stripping have been shown to be the dominant quenching mechanisms (e.g., Matharu et al. 2020, 2021; Werle et al. 2022).

In order to use structures to understand the quenching process, one would ideally like to track the evolution of poststarburst galaxies as a function of their time since quenching. However, precise timing of the time since quenching requires high-quality rest-frame optical spectra. Because the poststarburst population does not emerge significantly until $z \sim 1$ (Whitaker et al. 2012a; Wild et al. 2016), those spectra must be obtained at a minimum of intermediate redshift to catch even the tail end of the rapid quenching that dominates in the early universe. To date, spectroscopic studies of intermediateredshift post-starburst galaxies have been limited to small samples (e.g., Wu et al. 2018; Wild et al. 2020). However, spectroscopic samples of post-starburst galaxies at intermediate redshift are accessible in the Sloan Digital Sky Survey (SDSS) thanks in large part to the CMASS BOSS sample (Dawson et al. 2013), which targeted high-mass red galaxies at intermediate redshift. Leveraging this spectroscopic sample in addition to a handful of ancillary SDSS programs, we have launched the SQuIGG \vec{L} E survey (Suess et al. 2022), which spectroscopically identified 1318 post-starburst galaxies in the SDSS at z > 0.5 with spectral signatures that indicate that they have recently shut off their primary epoch of star formation. Crucially, these spectra allow us to characterize the properties of the burst to measure the time since star formation was quenched and to track the evolution of the sample in key properties as a function of the time since quenching. This sample has allowed us to study in detail the link between the star formation shutdown and active galactic nucleus (AGN) incidence (Greene et al. 2020), molecular gas content (Suess et al. 2017; Bezanson et al. 2022), and the incidence of mergers (M. Verrico et al. 2022, in preparation).

In this work and its companion letter (M. Verrico et al. 2022, in preparation), we match 145 post-starburst galaxies in the SQuIGGLE survey to deep imaging in the Hyper Suprime-Cam Survey (HSC; Aihara et al. 2018, 2022) in order to study their sizes, structures, and merger signatures and connect these properties to those of the star formation histories as derived from the SDSS spectroscopy. In Section 2, we introduce the SQuIGGLE sample and a mass-matched control sample of quiescent and star-forming galaxies to which we compare. In Section 3, we detail our methodology for measuring sizes and structures. In Section 4, we present our analysis of the sizes and structures. Finally, in Section 5, we discuss our results and their significance to understanding the rapid quenching pathway of galaxy evolution. Throughout this paper we assume a concordance Λ CDM cosmology with $\Omega_{\Lambda} = 0.7$, $\Omega_{m} = 0.3$ and $H_0 = 70 \text{ km s}^{-1} \text{ Mpc}^{-1}$, and quote AB magnitudes. All

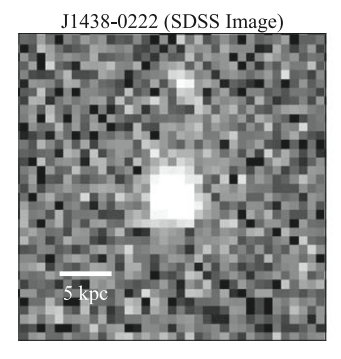




Figure 1. *i*-band images of J1438-0222, a z=0.698 post-starburst galaxy from the SDSS (left) and the HSC Wide Survey. The cutouts are centered at the same physical location, and the pixel scales are 0.396 and $0.1168 \, \mathrm{pixel}^{-1}$, respectively. The combination of better resolution and deeper images resolves faint, low-surface-brightness light that was previously inaccessible at this redshift, allowing us to accurately measure sizes and identify merger signatures.

reported values of the effective radius (r_e) are measurements of the semimajor axis and are not circularized.

2. Data

2.1. The SQuIGG \vec{L} E Sample

In order to study the descendants of the rapid quenching process, we turn to the SQuIGG \vec{L} E survey. The SQuIGG \vec{L} E sample is selected from the SDSS DR14 spectroscopic sample (Abolfathi et al. 2018) using the rest-frame U_m , B_m , and V_m medium-band filters from Kriek et al. (2010) to select galaxies with strong Balmer breaks (indicated by red $U_m - B_m$ colors) and blue slopes redward of the break (indicated by blue $B_m - V_m$ colors). In Suess et al. (2022), we show that this method reliably selects post-starburst galaxies that were quenched within the last $\sim 500 \,\mathrm{Myr}$, 75% of which formed >25% of their stellar mass in a recent burst, and further discuss the specific selection effects and how they differ from other post-starburst selection techniques. While SDSS imaging exists for the entire sample, the depth and resolution is not sufficient to resolve the galaxies. However, the HSC Wide Imaging Survey (Aihara et al. 2018) overlaps with \sim 10% of the galaxies in SQuIGG \vec{L} E and is deep enough to resolve the main galaxies in addition to faint structures, as seen in Figure 1.

In order to characterize the stellar populations of these galaxies, we perform two sets of SED modeling. The first, described in Setton et al. (2020), are performed on the the SDSS spectra and ugriz photometry using FAST++,¹⁴ an implementation of the FAST stellar population fitting code (Kriek et al. 2009). We assume a delayed-exponential star formation history (SFR $\sim te^{-t/\tau}$), BC03 stellar population libraries (Bruzual & Charlot 2003), a Chabrier (2003) initial mass function, and a Calzetti (1997) dust law. While these fits are limited to capturing only the recent burst of star formation in post-starburst galaxies due to the imposition of a single rise and fall in the star formation history, the physical measurements derived from this common parameterization can easily be compared to other galaxies in the literature that are fit similarly.

In addition to the traditional parametric fits, we perform nonparametric fits using a custom implementation of Prospector (Johnson & Leja 2017; Leja et al. 2017; Johnson

et al. 2021; see Suess et al. 2022 for details). These star formation histories impose their own set of priors on the stellar mass, which results in higher stellar masses than those derived with a delayed-exponential star formation history (e.g., Lower et al. 2020; Leja et al. 2021). In addition, nonparametric star formation histories are still only weakly constraining on star formation before the recent burst due to the outshining from the recently formed stellar population; as such, the prior chosen for early formation times significantly affects the conclusions about the burst mass fraction. However, these nonparametric fits are very useful for providing lower limits on the burst mass fraction with the conservative priors chosen, for robustly recovering the time since quenching, and for reliably measuring instantaneous star formation rates. For this work, we use the stellar masses derived from the delayed-exponential star formation history for consistency in comparisons to other mass-size relations, and employ the nonparametric star formation histories to investigate trends within the SQuIGG \vec{L} E post-starburst sample.

2.2. Coeval Control Sample from the LEGA-C Survey

In order to contextualize the sizes and structures of SQuIGGLE post-starburst galaxies relative to coeval starforming and quiescent galaxies, we require a sample of $z \sim 0.7$ galaxies with high-quality spectra that fully overlaps with the HSC. For this, we turn to the LEGA-C Survey DR3 (van der Wel et al. 2021). The LEGA-C Survey consists of deep (\sim 20 hr galaxy⁻¹) spectroscopy of galaxies in the Cosmological Evolution Survey (COSMOS) field. Because the SQuIGG \vec{L} E sample was selected from a variety of SDSS target selections with a variety of different color and magnitude cuts, we do not yet have a full understanding of how mass-complete or representative the sample of post-starburst galaxies are. As such, we elect to compare to a very conservative subset of LEGA-C galaxies above which completeness correction factors are negligible to ensure that the control population we are comparing to is fully representative of the galaxy population at $z \sim 0.7$. In this work, we use the subsample of LEGA-C galaxies with stellar masses (derived similarly to the SQuIGG \vec{L} E sample using delayed-exponential star formation histories) above $10^{10.7} M_{\odot}$, slightly higher than the characteristic mass of the sample and well into the regime where completeness corrections are ~ 1 (van der Wel et al. 2016). We divide the LEGA-C sample into quiescent and star-forming by their UVJ colors as in van der Wel et al. (2016) and use those samples as a control group to compare morphology and size measures to the post-starburst galaxies in SQuIGGLE, using similarly derived delayed-exponential star formation history masses.

The LEGA-C sample was selected using a redshift-dependent K-band magnitude cut, in contrast with SQuIGG \vec{L} E, which was selected using rest-frame colors and a signal-to-noise ratio cut from the whole of SDSS, largely from luminous red galaxies targeted using the CMASS selection criteria (Dawson et al. 2013). As such, the mass and redshift distributions of the two samples are different, even above the previously discussed stellar-mass threshold. In order to fairly compare structural measurements, we create a massmatched subsample of LEGA-C following the procedure described in detail in M. Verrico et al. (2022, in preparation). Briefly, for each galaxy in SQuIGG \vec{L} E, we select the quiescent and star-forming galaxy in LEGA-C that is within 0.05 dex in

¹⁴ https://github.com/cschreib/fastpp

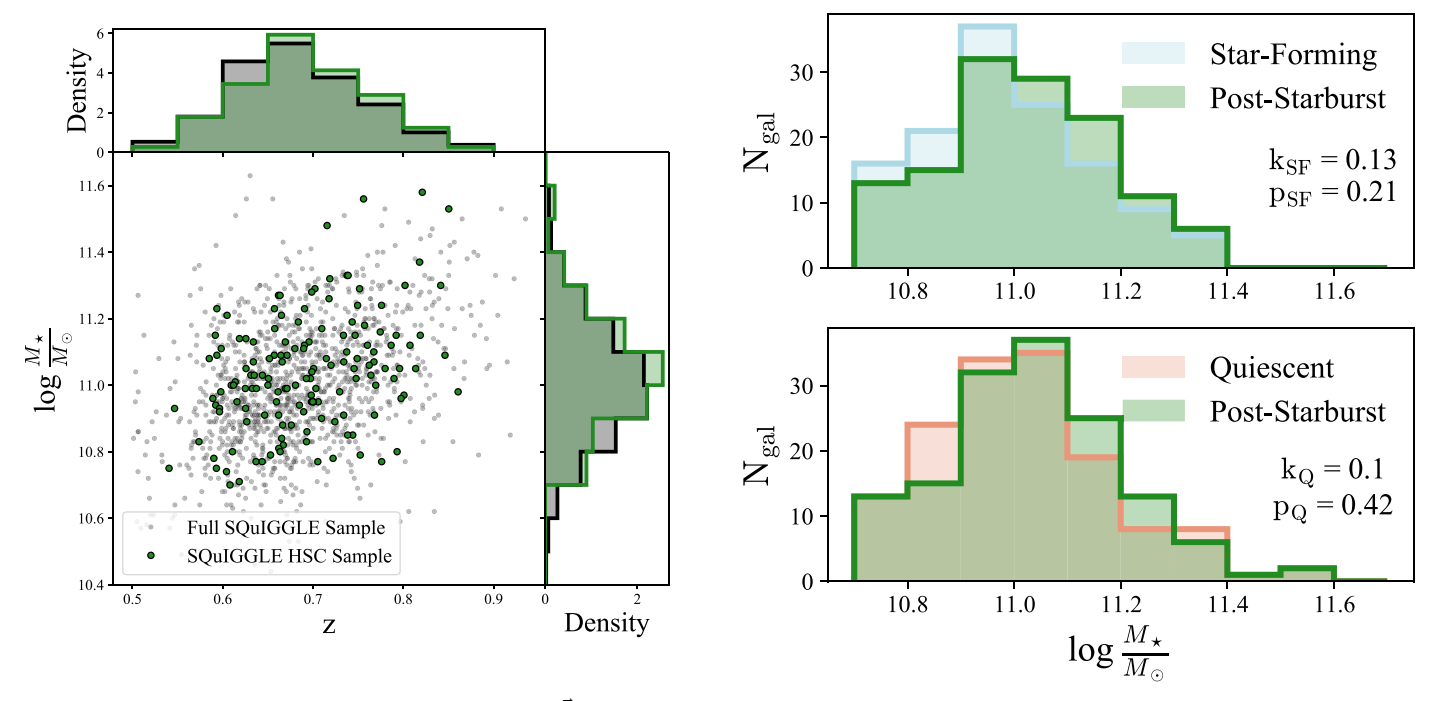


Figure 2. (Left) Stellar mass vs. redshift for the full SQuIGG \vec{L} E post-starburst sample (gray) and the HSC sample in this work (green). Above the mass cut of $M_{\star} > 10^{10.7} \, M_{\odot}$, the HSC sample spans the full range of SQuIGG \vec{L} E. (Right) The stellar-mass distributions for the mass-matched star-forming (blue) and quiescent (red) matches with the SQuIGG \vec{L} E sample. The samples are well matched in stellar mass, as indicated by the results of Kolmogorov–Smirnov tests on the two histograms.

stellar mass and is the closest in redshift to our main galaxy without replacement.

We perform this procedure on the full sample of SQuIGG \vec{L} E galaxies with high-quality HSC imaging (see Section 2.3) resulting in a final sample of 144 mass-matched pairs of poststarburst and quiescent and 129 pairs of post-starburst and starforming galaxies. For the 15 most massive galaxies in the SQuIGG \vec{L} E sample with high-quality HSC imaging, there is no similar-mass star-forming counterpart. This dearth of massive star-forming galaxies could be expected in a pencil-beam survey like LEGA-C given the steep high-mass end of the starforming stellar mass function (e.g., Muzzin et al. 2013). In addition, we are not able to match one of the most massive post-starburst galaxies to a quiescent counterpart. The results of the mass-matching procedure are shown as histograms in Figure 2(b). In both cases, a Kolmogorov–Smirnov test finds that the stellar mass distributions of the post-starburst and control samples are consistent with being drawn from the same distribution $(k_Q = 0.10, p_Q = 0.42; k_{SF} = 0.13, p_{SF} = 0.21).$ For the testing of size-fitting methodologies and the determination of the mass-size relations for star-forming and quiescent samples, we utilize the entirety of LEGA-C's mass-representative ($\log \frac{M_{\star}}{M_{\odot}} > 10.7$) sample. For all other comparisons, we utilize the mass-matched samples and show the star-forming matched post-starburst sample as dashed histograms for comparison with the star-forming distributions. We note that, by construction, the redshift distributions of the mass-matched samples, which were a secondary priority, overlap less precisely than those of the stellar masses. The LEGA-C quiescent and star-forming samples are a median 0.038 and 0.058 higher in redshift than SQuIGG \vec{L} E. We consider this

offset to be acceptable for the secondary parameter, as we are primarily interested in structural parameters of galaxies as they relate to the stellar mass, and the effects of surface brightness dimming are small over this narrow range in redshift.

In addition to fully overlapping with the HSC, the LEGA-C Survey has the added bonus of being fully observed with existing HST/ACS F814 imaging. This allows us to also use the galaxies in LEGA-C as a test to ensure that the inferences we make using ground-based data agree with the higher-resolution space-based data afforded by the Hubble Space Telescope (HST).

2.3. Hyper Suprime-Cam Imaging

In Figure 1, we show that the SDSS images of SQuIGG \vec{L} E galaxies are insufficient in both depth and resolution to study the structures of post-starburst galaxies at $z \sim 0.7$. However, imaging from the HSC survey (Aihara et al. 2018) can be used to robustly obtain sizes from the ground out to z < 1(Kawinwanichakij et al. 2021). As of PDR3, the HSC Wide Survey has taken data in at least one grizy band (Kawanomoto et al. 2018) of \sim 1300 deg² of the sky at depths \sim 3 orders of magnitude deeper than the SDSS (Aihara et al. 2022), making it ideal for the detailed study of SQuIGGLE post-starburst galaxy images. The survey design is such that the i band was observed to great depths (26.2 mag point-source limit), and, perhaps more importantly, at extremely high resolution (pointspread function FWHM ~ 0.06 , a factor of ~ 2 improvement over SDSS). As such, we elect to perform all our analysis on the i-band images that provide the best combination of depth and seeing and overlap with $\sim 10\%$ of the SQuIGGLE sample.

For every galaxy in SQuIGG \vec{L} E with *i*-band imaging in the HSC footprint, we pull a $48'' \times 48''$ coadd cutout and the corresponding point-spread function (PSF) model from the PSF Picker 15 (Bosch et al. 2018). After performing the same mass cut $(\log \frac{M_{\star}}{M_{\odot}} > 10.7)$ as on LEGA-C, we find that 150 SQuIGG \vec{L} E galaxies have been imaged in the HSC *i* band. We visually inspect all galaxies and exclude images with clear visual artifacts (e.g., cosmic rays, image streaks) in the region of the central object, as well as objects with extremely bright nearby sources that significantly alter the sky subtraction. This removes 5/150 galaxies with HSC coverage, leaving us with a total of 145 post-starburst galaxies with clean images. A full gallery of the SQuIGG \vec{L} E sample cutouts is shown in M. Verrico et al. (2022, in preparation). The results of this selection in the mass–redshift plane are shown in Figure 2. The subset of SQuIGGLE galaxies we study in this work spans the range of the full SQuIGG \vec{L} E sample above the masscompleteness cut.

In addition, we pull cutouts using the identical procedure as above for the entirety of the LEGA-C mass-representative sample. The HSC survey consists of three sky layers: wide, deep, and ultra deep, covering 1400 deg², 26 deg², and 3.5 deg², respectively, and each \sim 1 dex deeper than the shallower layer (Aihara et al. 2018). Every galaxy in SQuIGG \vec{L} E was observed only at wide depth; however, the LEGA-C field overlaps with the deep layer of HSC. In order to facilitate a fair comparison to the SQuIGG \vec{L} E sample, we utilize the widedepth reductions of the LEGA-C galaxies to ensure that the surface brightness limits are similar between the two samples. However, we also pull the full-depth HSC Deep cutouts and PSF models for the entire sample, which we use to test the reliability of our fitting procedures for deeper images.

2.4. Tidal Feature Classifications

In M. Verrico et al. (2022, in preparation), we present visual classifications of the incidence of tidal features in the massmatched SQuIGGLE and coeval LEGA-C samples. In brief, we instructed eleven members of the SOuIGG \vec{L} E team and the Pitt Galaxy Group to assign a binary classification of "Tidally Disturbed" or "Not Disturbed" to postage stamps of the SOuIGGLE and mass-matched LEGA-C control samples in random order. We divide galaxies into three categories: disturbed (>70% agreement that a tidal feature is present, $N_{\rm gal}\!=\!61$), nondisturbed (>70% agreement that no tidal features are present, $N_{\rm gal}\!=\!51$), and ambiguous (all galaxies that meet neither of these conditions, often due to the presence of neighbors where the association is unclear and rankers were divided, $N_{\rm gal} = 33$). Throughout this work, we utilize the disturbed and nondisturbed subsamples of SQuIGGLE to test whether structural parameters vary based on whether or not a galaxy has clear tidal features.

3. Galaxy Size and Structure Fitting

3.1. Measuring Sérsic Sizes

We utilize GALFIT (Peng et al. 2010) to quantify the structural parameters of SQuIGG \vec{L} E post-starburst galaxies and the LEGA-C control sample. For each image, we identify and deblend all light sources detected at the 5σ level above the

background using the Python astropy photutils package (Astropy Collaboration et al. 2013, 2018), using the following settings, which were chosen to optimally deblend based on visual inspection of the resultant segmentation maps:

```
fwhm_smooth = 3
sigma_detect = 3
npixels = 5
npixels_deblend = 5.
```

We use the source_properties function to extract approximate centroids, axis ratios, position angles, and fluxes of each source. We then mask all sources greater than 25 pixels (4"2) from the center of the image and any objects within the central 25 pixels that are more than three magnitudes fainter than the central object. We smooth the resultant mask with a 3 pixel radius top-hat filter in order to ensure that we are accounting for all galaxy light from all interloping sources. These aggressive masking choices were made to ensure that all bright nearby sources are being accounted for with their own models and that the Sérsic profiles are sensitive to the smooth central profiles of the galaxies. To this end, we elect in our deblending parameters to err on the side of classifying spatially distinct tidal features, such as the one to the northwest of the galaxy in Figure 4, as their own objects and to mask them, biasing the sizes of all galaxies we fit toward smaller values.

We then allow GALFIT to fit the object of interest and the remaining neighboring galaxies (those within 25 pixels and within 3 mag of the central object) with Sérsic profiles convolved with the PSF. We adopt the bounds on the Sérsic index 0.5 < n < 6 following the most recent LEGA-C data release to facilitate comparisons to their fits using HST Advanced Camera for Surveys (ACS) F814 images (van der Wel et al. 2021). The centroid, position angle, axis ratio (b/a), and magnitudes measured by photutils are used as initial guesses for the parameters in the Sérsic fits for each object. The sky background is initialized at 0 and is a free parameter in the fit. In Figure 3, we demonstrate the full Sérsic fitting procedure on a SQuIGG \vec{L} E galaxy that has a nearby source that meets our criteria for simultaneous fitting. The nearby source immediately to the south of the galaxy of interest is too faint to be fit, and as such appears in the mask, but the source to the northeast is bright enough to be fit with its own Sérsic model. The bestfitting Sérsic parameters from these fits are detailed in Table 1.

In Greene et al. (2020), we find that \sim 5% of SQuIGGLE post-starburst galaxies host AGN, which are identified via their strong [O III]/H_{β} ratios. However, in all cases the narrow lines indicate that the AGN are strongly obscured and should not significantly impact the rest-frame optical continuum of the galaxies. As such, we do not elect to fit any additional point-source components to the six AGN in our sample. Throughout this work, we report the semimajor effective radius (r_e) as the measure of galaxy size.

Although the LEGA-C control sample is covered by the deeper HSC Deep imaging, SQuIGG \vec{L} E galaxies fall entirely within the shallower HSC Wide footprint. In order to compare morphological measurements fairly to SQuIGG \vec{L} E, we utilize imaging for the LEGA-C control sample (galaxy postage stamps and PSFs) of the HSC Deep field that is only stacked to Wide depths. To assess the reliability of our structural measures, we compare the results from HSC fits for the LEGA-C sample to structural parameters measured from HST/ACS F814W imaging in van der Wel et al. (2021) in

https://hsc-release.mtk.nao.ac.jp/psf/pdr3/

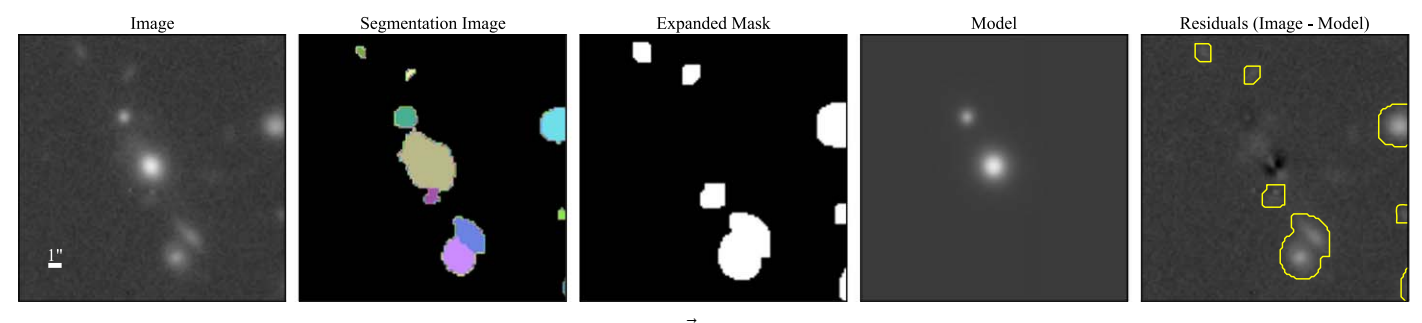


Figure 3. Demonstration of the multicomponent fitting procedure on a SQuIGG \vec{L} E post-starburst galaxy. We first show the unmasked image centered on the galaxy of interest in a $20'' \times 20''$ cutout, with nearby interlopers. The second panel demonstrates the source identification procedure described in Section 3.1, which successfully detects and deblends all sources in the field of view. The third panel shows the mask that we provide to GALFIT, which is the segmentation map for all sources >25 pixels from the galaxy of interest or that are within 25 pixels but are 3 dex fainter than the main source convolved with a 3 pixel top-hat kernel. Note that the object to the northeast of the galaxy of interest is bright and close enough to not be masked. In the fourth panel, we show the best-fitting model produced by GALFIT, and in the final panel we show the residuals on the same color scale as the image and the model, with the masked regions outlined. The fitting successfully accounts for the majority of the light from both the main galaxy and the neighbor.

 $\textbf{Table 1} \\ \textbf{Structural and Selected Spectrophotometric Properties of SQuIGG\vec{L}E Post-starburst Galaxies}$

Name	$z_{\rm spec}$	$\log(\frac{M_{\star}}{M_{\odot}})^{\mathrm{a}}$	r _{e,Sersic} (kpc) ^b	r _{e,corr} (kpc) ^c	n^{b}	mag ^b	b/a ^b	$\log(\Sigma_{1 \text{ kpc}})^{b}$	G^{d}	GC ^d	$t_q (\mathrm{Gyr})^{\mathbf{e}}$	Burst Fraction ^e
J1042+0500	0.6266	$10.89 \pm ^{0.01}_{0.02}$	0.78	0.76	5.98	19.61	0.94	10.16	0.59	2.5	$0.31 \pm^{0.09}_{0.1}$	$0.52 \pm^{0.21}_{0.12}$
J0907+0423	0.6635	$11.27 \pm ^{0.01}_{0.02}$	7.03	6.06	3.47	19.25	0.85	9.81	0.5	2.97	$0.11 \pm ^{0.08}_{0.04}$	$0.36 \pm_{0.2}^{0.58}$
J0226+0018	0.5405	$10.75 \pm ^{0.03}_{0.03}$	2.09	2.09	6.0	19.26	0.89	9.83	0.63	2.67	$0.36 \pm^{0.13}_{0.13}$	$0.44 \pm^{0.34}_{0.17}$
J0224-0105	0.5979	$10.98 \pm ^{0.01}_{0.02}$	3.36	3.21	5.76	18.82	0.81	9.97	0.64	2.84	$0.39 \pm^{0.18}_{0.11}$	$0.88 \pm^{0.12}_{0.62}$
J0221-0646	0.6613	$10.98 \pm ^{0.02}_{0.02}$	5.58	5.82	5.56	19.46	0.67	9.88	0.51	2.64	$0.22 \pm ^{0.08}_{0.07}$	$0.27 \pm^{0.28}_{0.08}$

Notes.

(This table is available in its entirety in machine-readable form.)

Appendix A. We find that our fits are very reliable despite the images being lower in resolution by a factor of ~ 3 compared to the HST/ACS F814W imaging. In many cases, the increased low-surface-brightness sensitivity of HSC better captures the wings of galaxy profiles at large radii. This difference in profiles can explain the systematic offsets in the Sérsic index and the effective radius. We find that we recover the axis ratio with extremely high precision and accuracy (median $\Delta b/a = 0.005$, $\sigma_{\Delta b/a} = 0.11$).

We also test the robustness of our fits by comparing to analysis of HSC Deep imaging for the LEGA-C sample. We find that our measurements of the effective radius between the Deep and Wide are extremely consistent, with a median offset of 0% and a scatter of $\sim\!8\%$ in measured size. Axis ratios are similarly well constrained, with a scatter $\sigma_{b/a} \sim 0.02$. The median Sérsic index fit with the Deep images is found to be slightly lower than with Wide, with $\Delta n = -0.05$, $\Delta n_{16\%} = -0.45$, and $\Delta n_{84\%} = 0.15$. We conclude that the HSC Wide images are sufficient for robustly measuring sizes of massive galaxies at intermediate redshift.

We also use the derived Sérsic profiles to compute the stellar mass surface density within one kiloparsec ($\Sigma_{1 \text{ kpc}}$). We do so by multiplying the fraction of the flux contained within 1 kpc by the galaxy stellar mass and dividing by the area of the

bounding ellipse using the best-fitting Sérsic profile parameters, implicitly assuming a flat M/L gradient

$$\Sigma_{1 \text{ kpc}} = \frac{M_{\star} \frac{f_{1 \text{ kpc}}}{f_{\text{tot}}}}{\pi (1 \text{ kpc})^{2} (b/a)}.$$
 (1)

3.2. Systematic Size Errors due to PSF Models

The formal uncertainties on the sizes for bright galaxies measured using GALFIT are very small because the HSC images are so high in signal-to-noise ratio. However, these formal uncertainties ignore potentially significant systematic errors. Likely the largest systematic is the assumption that the PSF model used in the Sérsic model fitting is well determined at any point in the sky. As galaxies at intermediate redshift have intrinsic sizes similar to the full width at half maximum of the point-spread function, small changes in the shape of the PSF can lead to significantly different measurements of galaxy size and Sérsic index.

In order to account for this, for each galaxy in SQuIGGLE we sample the PSF from the HSC PSF Picker at 50 locations drawn from a normal distribution surrounding the galaxy with $\sigma = 0^{\circ}.375$ in R.A. and decl. This choice of σ ensures that we will be picking PSFs that are distributed throughout the entire

^a Stellar masses were derived using a delayed-exponential star formation history, described in Section 2.1.

b Sérsic parameters were derived using single-component 2D Sérsic models to fit the galaxies of interest. Uncertainties derived by refitting the galaxies using a range of PSF models from nearby locations on the sky are shown in Table 2. For details, see Section 3.1.

^c The residual-corrected effective radii were derived using the method of Szomoru et al. (2012), described in Section 3.3.

d The Gini coefficient (G) and the generalized concentration (GC) were measured on the segmentation maps described in Section 3.1, for details see Section 4.3.

^e The time since quenching (t_q) and the burst fraction are model parameters derived from nonparametric star formation history fitting of the galaxies, see Suess et al. (2022) for details.

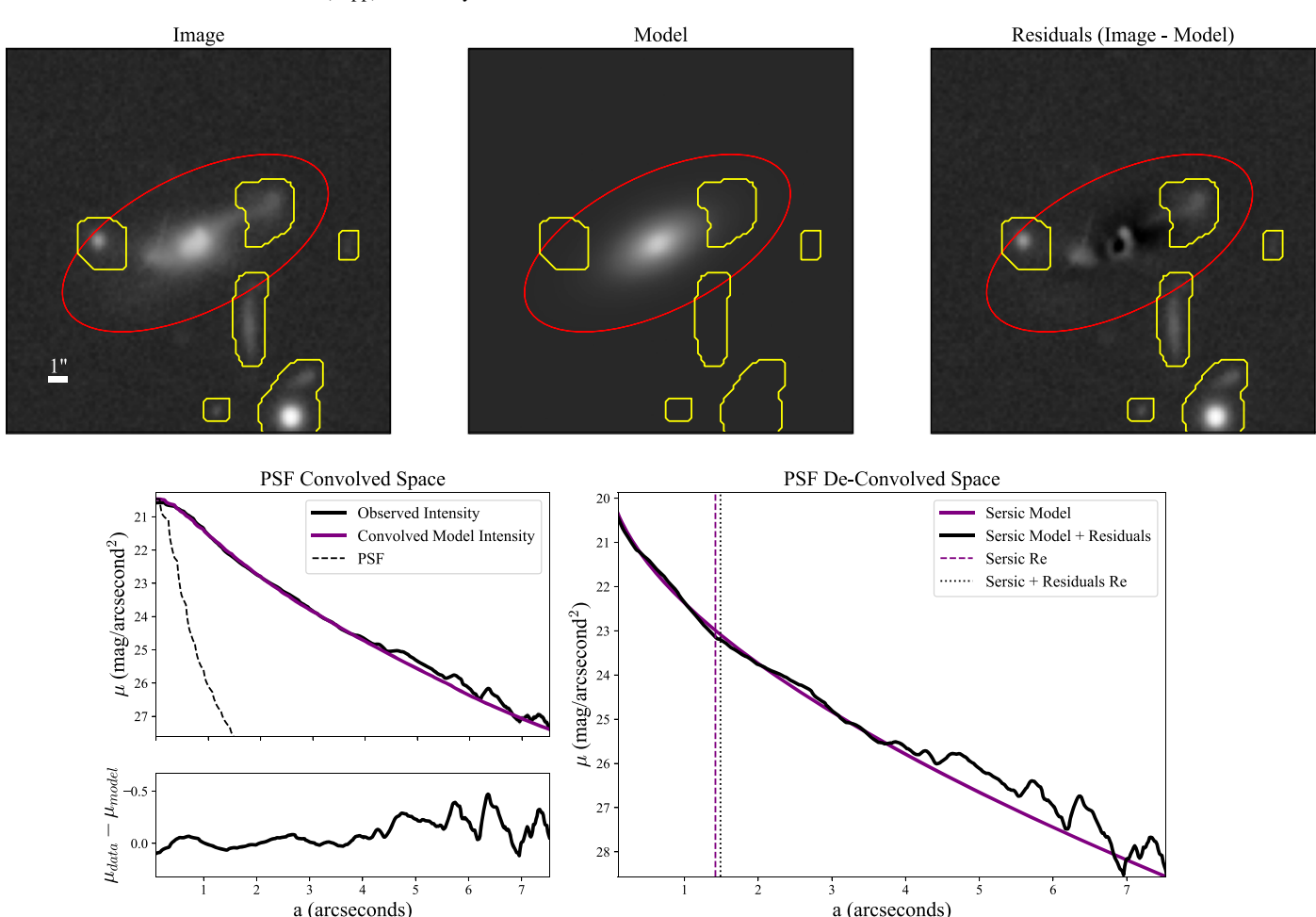


Figure 4. (Top) Image, best-fitting Sérsic model, and resulting residuals of a SQuIGG \vec{L} E post-starburst galaxy that exhibits clear merger features, some of which are masked (yellow outlines) in our source identification algorithms. The red aperture indicates the largest annulus used in extracting a 1D surface brightness profile, corresponding to the point where the signal-to-noise ratio drops below 5. (Bottom left) Observed (black) and model (purple) radially averaged surface brightness profiles as a function of the semimajor axis of the best-fitting ellipse, with residuals shown below. The Sérsic model underestimates the surface brightness at large radii. (Bottom right) The same model (purple) as the center, now shown without PSF convolution. The same profile is shown with the residuals added to them using the method from Szomoru et al. (2012). The dashed and dotted lines represent the effective radius of the profile before and after this addition takes place. While the residuals do affect the total shape of the profile, the measurement of the effective radius is largely robust to this correction.

 Table 2

 Uncertainties on Sérsic Parameters from PSF Model Refitting

Name	r _e (kpc)			n			mag			b/a			$\log(\Sigma_{1 \text{ kpc}})$		
	16%	50%	84%	16%	50%	84%	16%	50%	84%	16%	50%	84%	16%	50%	84%
J1042+0500	0.94	1.3	1.62	2.72	3.09	5.82	19.64	19.66	19.67	0.74	0.82	0.94	9.94	10.02	10.1
J0907+0423	6.98	7.3	8.28	3.21	3.51	4.64	19.16	19.24	19.26	0.84	0.86	0.89	9.71	9.73	9.8
J0226+0018	2.25	2.37	2.48	4.02	5.32	6.0	19.25	19.27	19.31	0.82	0.86	0.9	9.69	9.74	9.76
J0224-0105	3.04	3.22	3.29	4.86	5.63	6.0	18.82	18.84	18.87	0.78	0.8	0.83	9.86	9.88	9.91
J0221-0646	5.39	5.58	5.83	5.16	5.6	6.0	19.44	19.45	19.47	0.68	0.71	0.74	9.68	9.7	9.72

(This table is available in its entirety in machine-readable form.)

1.5 field of view of HSC surrounding the object of interest. At each position, the PSF is estimated based on surrounding stars, and the distribution in the shapes of these PSFs should approximate the uncertainty in the determination of the PSF at the position of the galaxy itself.

We refit each galaxy with each of the 50 randomly drawn PSFs and quantify the error in the measurement of the effective

radius. We find that the uncertainties from this PSF shuffling are an order of magnitude larger than the formal uncertainties (median $\sigma_{\text{re,formal}} = 0\rlap.{''}004$, median $\sigma_{\text{re,PSF}} = 0\rlap.{''}049$). We take these systematic errors to be dominant and throughout the rest of the work, all errors reported in the size result from this methodology. For each of the 50 iterations, we also calculate $\log(\Sigma_{1 \text{ kpc}})$, for which we find a median error of 0.05 dex. The

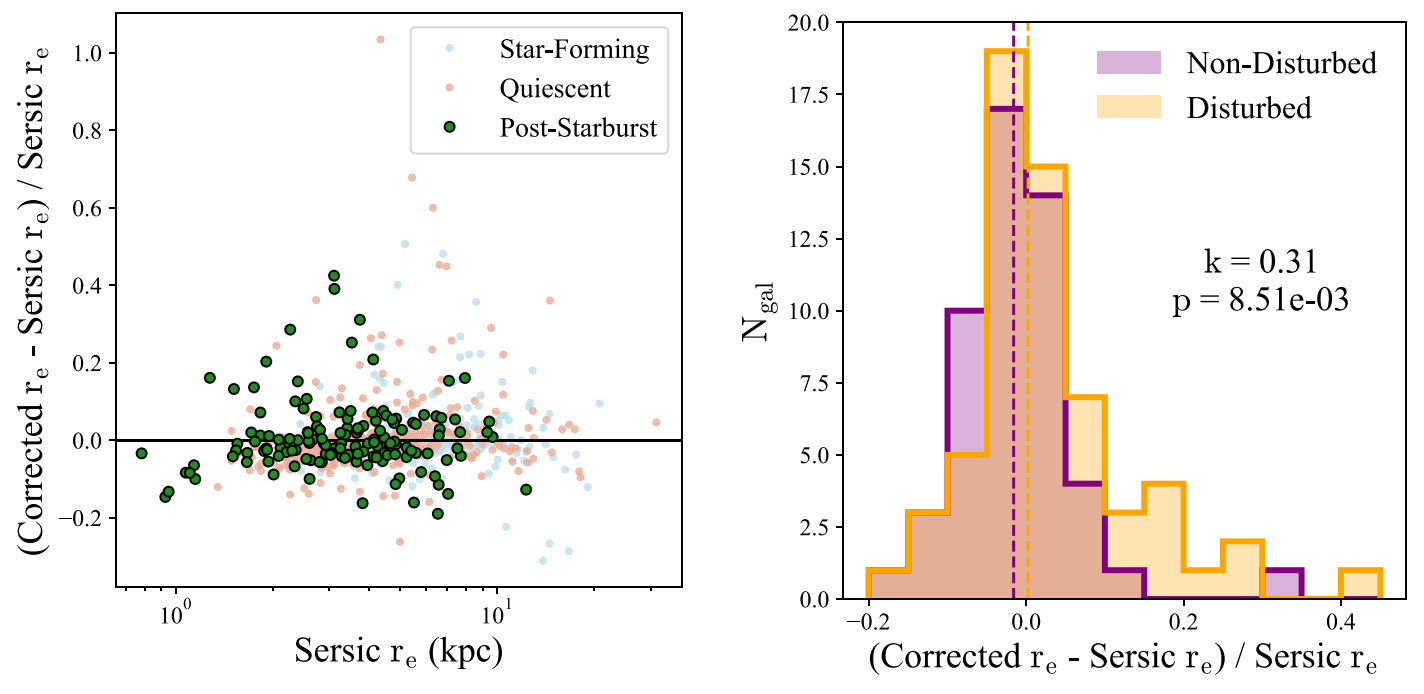


Figure 5. (Left) Measured Sérsic effective semimajor axis radius from GALFIT vs. residual-corrected percent error in r_e from the application of the Szomoru et al. (2012) technique to post-starburst galaxies in SQuIGG \vec{L} E and quiescent/star-forming galaxies from the LEGA-C survey. Globally, the addition of the residuals only biases measurements to be \sim 1% smaller, and the majority of galaxies have measured sizes consistent within \sim 10%. (Right) Distributions of the residual-corrected percent error in r_e for the disturbed and nondisturbed post-starburst samples. The median offsets in the measured sizes (vertical lines) for the samples are comparable, but the majority of the galaxies where the corrected sizes are significantly larger are visually flagged as tidally disturbed.

full 1σ confidence intervals in Sérsic properties inferred from the PSF refitting are shown in Table 2.

3.3. Accounting for Non-Sérsic Light

Sérsic profiles can provide average properties of the smooth 2D light distributions of galaxies (e.g., van der Wel et al. 2012; Almaini et al. 2017; Wu et al. 2018; Mowla et al. 2019; Kawinwanichakij et al. 2021). However, the Sérsic model does not fully account for asymmetric light from tidal features, which are present in many galaxies and are very common in the SQuIGG \vec{L} E sample of post-starburst galaxies in deep imaging (see M. Verrico et al. 2022, in preparation) and are not fully masked even in our conservative source identification procedure (see Figure 4). Additionally, single-component Sérsic fits need not perfectly describe the profiles of isolated galaxies; for example, the presence of a bright point-source component (which we do not expect from AGN but could potentially result from nuclear star formation) could drive a fit to be overly peaked, missing light in the wings of the galaxy as a result. These deviations in the Sérsic fits from the true surface brightness profiles of galaxies can bias inferences about the sizes of galaxies; accounting for it is important in accurately comparing to the sizes of coeval galaxies.

We follow Szomoru et al. (2012) to correct for deviations from Sérsic profiles, including asymmetries, while accounting for PSF smearing. To start, we run GALFIT on galaxies as described in Section 3.1. We begin by performing annular photometry on the residual (galaxy image minus the best-fitting Sérsic models of *all* simultaneously fit galaxies multiplied by a mask that masks all nonprimary sources, including those that were fit simultaneously) using the best-fitting position, position angle, and axis ratios derived from the Sérsic fits. We extract the profiles out to the annulus where the signal-to-noise ratio in the galaxy image drops below 5, ~28 mag arcsec⁻². We add

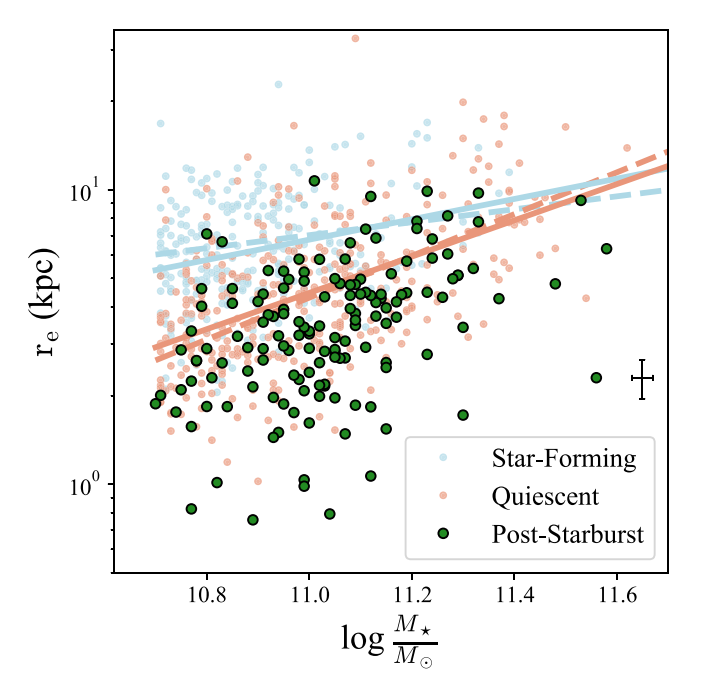


Figure 6. Effective radius vs. stellar mass relation for $z \sim 0.7$ post-starburst (green), quiescent (red), and star-forming (blue) galaxies. Characteristic error bars in the mass and size are shown in black. The best-fitting relations to star-forming and quiescent galaxies (blue and red respectively) are shown as solid lines. Best fits from van der Wel et al. (2014) for 0.5 < z < 1.0 are shown as dashed lines. SQuIGG \vec{L} E post-starburst galaxies are compact on average relative to both star-forming and quiescent galaxies, though there is significant scatter within each population.

these PSF-convolved residuals to the *deconvolved* best-fitting Sérsic profile and remeasure the half-light radius from the residual-corrected growth curve. An illustration of this method is shown in Figure 4 for a clearly disturbed galaxy. Even in this

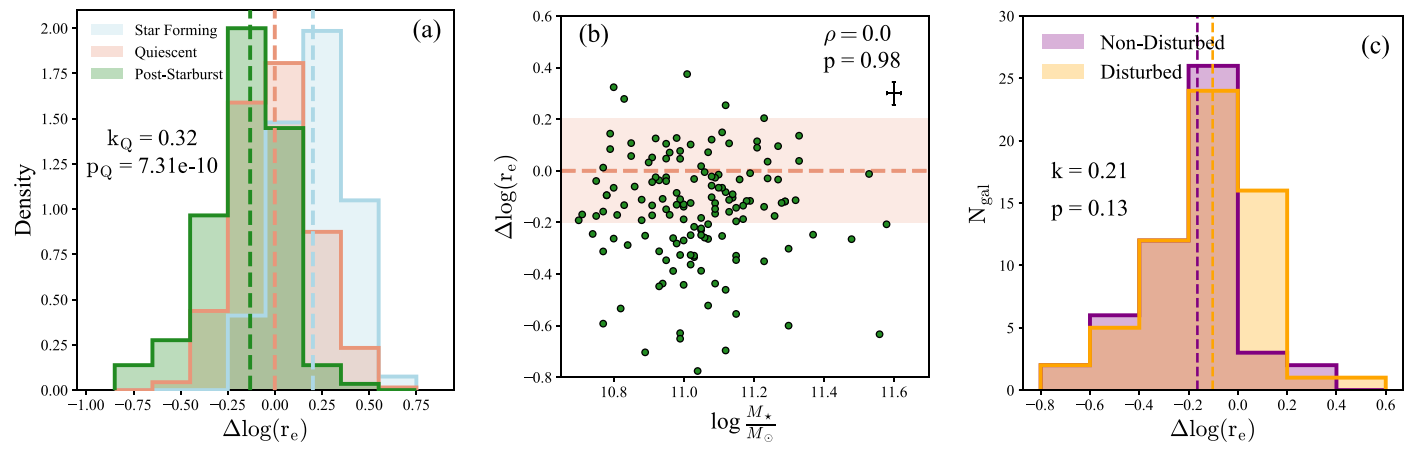


Figure 7. (Left) Distribution of $\Delta \log(r_e)$ from the quiescent mass–size relation for the star-forming (blue), quiescent (red), and post-starburst (green) samples. The medians of the samples are indicated with vertical dashed lines. The star-forming sample is a median ~ 0.2 dex larger than the quiescent sample at a given stellar mass. The post-starburst sample is a median of 0.13 dex below the quiescent population. All three samples have similar scatter of ~ 0.2 dex. (Center) $\Delta \log(r_e)$ vs. $\log M_{\star}$ for the SQuIGG \vec{L} E post-starburst sample (green). The red dashed line and shaded region represent the quiescent mass–size relation. Typical errors are shown as in black. Post-starburst galaxies uniformly scatter below quiescent galaxies, with no trend as a function of the stellar mass as evidenced by the Spearman correlation coefficient (ρ) and associated p-value. (Right) Distributions in $\Delta \log(r_e)$ for the nondisturbed an disturbed samples of post-starburst galaxies as defined in M. Verrico et al. (2022, in preparation). While the median size at fixed stellar mass is slightly smaller than for the nondisturbed sample, a Kolmogorov–Smirnov test shows that the samples are consistent with being drawn from the same distribution (see associated k and p values).

extreme case, the tidal features do not contribute significantly to the total galaxy flux and the measured size is only 5% larger than the Sérsic effective radius.

In general, the residual-corrected sizes do not deviate significantly from the corresponding Sérsic effective radii. We show this in Figure 5(a), comparing the sizes measured with GALFIT to the residual-corrected sizes. While we find that in a few cases, the residual-corrected sizes are significantly (≥25%) larger than those measured by Sérsic fits, the median deviation from Sérsic is $\sim -1\%$ for star-forming, quiescent, and post-starburst galaxies, indicating that non-Sérsic and asymmetric light is not significantly affecting galaxy sizes. The majority of the measurements that skew toward significantly larger sizes are due to the presence of tidal features along the semimajor axis (see Figure 5(b)). We adopt these corrected effective radii as our measure of galaxy sizes for the remainder of this work. However, due to the lack of systematic offsets in any of the samples, all conclusions in this work would not change if we were to use the Sérsic-only half-light sizes.

4. The Sizes and Structures of Post-starburst Galaxies

4.1. Post-starburst Half-light Sizes

Across redshift, star-forming, and quiescent galaxies exhibit differing relations in the size-mass plane when size is quantified by the half-light radius (van der Wel et al. 2014; Wu et al. 2018; Mowla et al. 2019). The sizes of galaxies scale with their stellar mass, but quiescent galaxies are generally smaller and follow a steeper relation than star-forming galaxies. In this section, we hope to constrain the rapid path to quiescence by comparing the sizes of coeval post-starburst, quiescent, and star-forming galaxies. In Figure 6, we show the residualcorrected effective radius versus mass for the SQuIGGLE poststarburst galaxies in green, along with the mass-representative $(\log \frac{M_{\star}}{M_{\odot}} > 10.7)$ LEGA-C star-forming (blue) and quiescent (red) samples. The blue and red solid lines are our best-fitting relations for star-forming and quiescent galaxies, respectively, and the dashed lines are the best-fitting relations from van der Wel et al. (2014). There is considerable scatter in the sizes of the post-starburst galaxies, but on average they are fairly compact relative to all of the LEGA-C sample.

In order to test the relative compactness of post-starburst galaxies, we define $\Delta \log(r_{\rm e})$, the vertical offset with regard to the quiescent mass-size relation, $\hat{r}_{\rm e}$, $Q(\log \frac{M_{\star}}{M_{\odot}})$, as follows:

$$\Delta \log(r_e) = \log(r_e) - \log(\hat{r}_e, Q(\log \frac{M_*}{M_\odot})). \tag{2}$$

In Figure 7(a), we show the distributions in $\Delta \log(r_e)$ of the SQuIGGLE post-starburst galaxies in green in addition to the quiescent (red) and star-forming (blue) mass-complete samples. All three populations show similar scatter (\sim 0.2 dex), but the SQuIGGLE galaxies ~ 0.1 dex more compact in their light distributions than quiescent galaxies at similar redshift. In order to quantify the uncertainty in the inferred median $\Delta \log(r_{\rm e})$, we refit the quiescent mass-size relation using the emcee implementation of Markov Chain Monte Carlo (Foreman-Mackey et al. 2013) and draw randomly from the posterior for the intercept and slope. We find a 1σ confidence interval on the median value of $\Delta \log(r_e)$ of [-0.17, -0.07]. In Figure 7(b), we show that the offset from this sequence does not correlate with the mass of the galaxy. We perform a two-sample Kolmogorov–Smirnov test on $\Delta \log(r_e)$ for the post-starburst and quiescent samples find that they are not consistent with being drawn from the same distribution ($p = 2.57 \times 10^{-4}$). In addition, we perform a 2D Kolmogorov-Smirnov test (Peacock 1983; Fasano & Franceschini 1987) on the mass-matched mass-size plane to ensure that this conclusion is robust to our definition of $\Delta \log(r_e)$. This test confirms that post-starburst galaxies are not consistent with being drawn from the same 2D distribution as the quiescent galaxies ($p = 7.95 \times 10^{-4}$).

The compact sizes we measure for the post-starburst sample relative to coeval quiescent and star-forming populations are broadly consistent with the smaller-than-average coeval post-starburst galaxies selected from the LEGA-C survey (Wu et al. 2018, 2020) in addition to high-mass ($M_{\star} > 10^{10} \, M_{\odot}$) post-starburst galaxies at 1 < z < 2 (Yano et al. 2016; Almaini et al. 2017; Maltby et al. 2018). The light-weighted sizes are also similarly compact to the $M_{\star} \sim 10^{11} \, M_{\odot}$ post-starburst galaxies

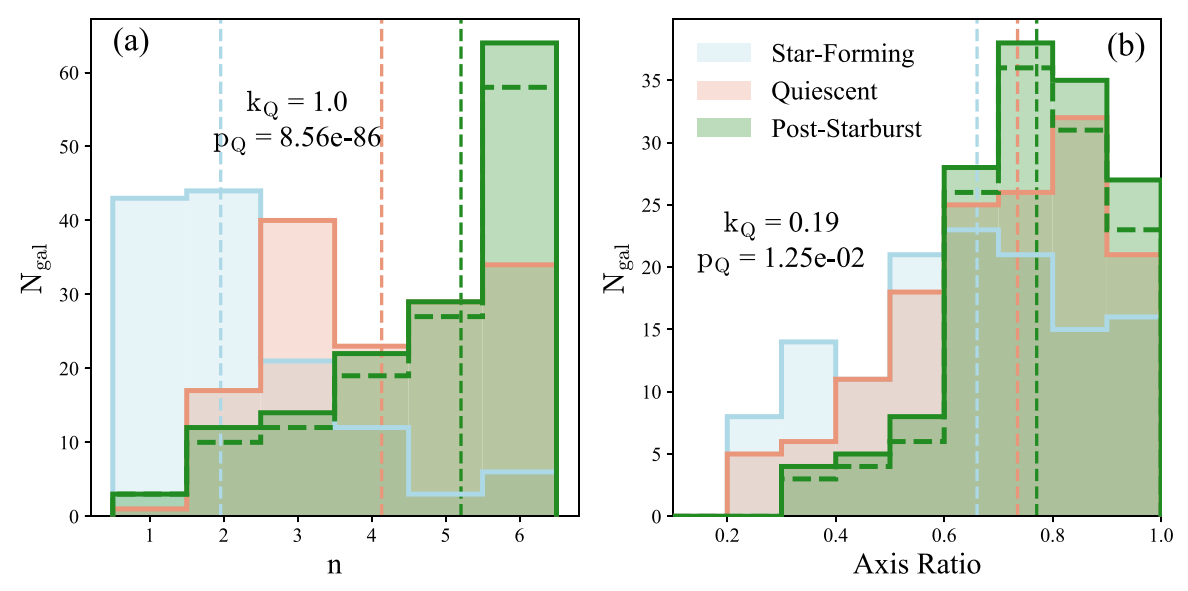


Figure 8. (Left) Distributions of mass-matched post-starburst (green), star-forming (blue), and quiescent (red) galaxies for the Sérsic index n. The dashed post-starburst histogram shows the post-starburst galaxies that are mass-matched to the star-forming sample. Post-starburst galaxies have an overwhelming fit with large n, often running up against the n = 6 boundary. The Sérsic index distribution is distinct from that of star-forming galaxies, which favor small n. (Right) Distributions of axis ratios, defined as the ratio of the semiminor axis to the semimajor axis. Star-forming galaxies show the most elongation, followed by quiescent galaxies, and post-starburst galaxies are slightly rounder than both. In both plots, the median of each distribution is shown as a dashed vertical line. The results of a Kolmogorov–Smirnov test between the quiescent and post-starburst distributions are shown on both figures.

in Suess et al. (2020). In Figure 7(c), we show the distributions in $\Delta \log(r_e)$ splitting the sample into disturbed and nondisturbed using the classifications from M. Verrico et al. (2022, in preparation). While the median size at fixed stellar mass is slightly larger for the disturbed population (owing to the fact that tidal features do influence the effective radius), a Kolmogorov–Smirnov test shows that the distributions do not differ significantly, and the entire post-starburst sample is compact relative to coeval quiescent galaxies.

Crucially, we note that these galaxies are resolved in the HSC imaging. In Appendix A, we demonstrate that the sizes we measure using HSC imaging of galaxies at this redshift are almost entirely consistent with the sizes measured on the smallest galaxies in van der Wel et al. (2021), and in Appendix B we demonstrate that the 1D and 2D surface brightness profiles of the smallest galaxies in SQuIGG \vec{L} E are significantly different from that of the PSF. In the i band, the light of the youngest stellar population will almost completely dominate over any older stellar population, and so the sizes we measure are likely to primarily trace the physical extent of that population. This finding indicates that the recent star formation was extended on at least kiloparsec scales past the circumnuclear region in all the galaxies in our sample.

4.2. Other Parametric Measures of Structure

In addition to the half-light radius, the Sérsic models also include the Sérsic index (n) and the projected axis ratio (b/a) in the 2D fits to the galaxies. These structural measures encode information about the 3D structures and light profiles of galaxies and show different empirical trends for star-forming and quiescent populations (e.g., Shen et al. 2003; van der Wel et al. 2014). In Figure 8, we show the distributions in the Sérsic index and the axis ratio for post-starburst galaxies, as well as the mass-matched quiescent and star-forming control samples. As expected, the star-forming sample and the quiescent sample are significantly different in their Sérsic index distributions;

star-forming galaxies are fit with small Sérsic index $(n_{\text{med}} \sim 2)$ and quiescent galaxies are systematically fit with higher n $(n_{\rm med} \sim 4)$. Post-starburst galaxies have higher Sérsic indices than both of these samples, with a median Sérsic index of 5.2. These higher Sérsic indices are likely driven by the concentrated light of these objects, and visual inspection of the median 1D surface brightness profiles of the sample confirms that the majority of the galaxies are being well fit by these high Sérsic indices. We note, however, that many poststarburst and quiescent galaxies run up against the boundary we impose at n = 6. We run a number of tests including residual inspection, fitting images with a central point-source component in addition to a Sérsic profile, and expanding the threshold Sérsic index to n = 8, in order to quantify the effects of the run-up against the boundary to our results. Ultimately, the qualitative results of the paper are insensitive to any changes to our fitting procedure, but we describe these tests below.

For the sample of SQuIGGLE post-starburst galaxies, 36% galaxies run up against the n = 6 boundary, whereas in the mass-matched quiescent sample 20% of the galaxies are best fit with n = 6. In general, the Sérsic index is the least well constrained property in our fits, as it is extremely sensitive to the shape of the PSF model we use in fitting. Additionally, these uncertainties grow as a function of the best-fitting Sérsic index, such that for galaxies with intrinsically high Sérsic indices (e.g., quiescent and post-starburst galaxies), the Sérsic indices are particularly poorly constrained. Visual inspection of the residual 1D surface brightness profiles of the galaxies that run up to the n = 6 boundary show that, in contrast with the rest of the sample, these have median central mismatches of $-0.04 \text{ mag arcsec}^{-2}$. The models are systematically fainter in the center than the galaxies and brighter than the galaxies on scales of $\sim 1''$. This imperfect agreement between data and model is what we would expect from a mismatch between the model PSF we use in the fitting of the galaxies and the true PSF of the galaxies, where the centrally concentrated light of the

galaxies is smeared by a PSF that is wider than the true PSF. In some cases (e.g., galaxy J0226+0018 in Tables 1 and 2), a nearby PSF model is capable of causing the fit to converge to a Sérsic index that is within the range we allow, but in many cases all 50 fits in our rerun with nearby PSF models converge to the same n = 6 value.

This issue of high-*n* pileup cannot be resolved by simply expanding the Sérsic index to higher values. We rerun our fits of the SOuIGGLE sample with an upper boundary on the Sérsic index of n = 8 and find that 20% of the galaxies still converge to the upper boundary and show the same characteristic residual shape as in the n = 6 boundary fits, indicating that the light is generally not well fit by a Sérsic profile regardless of the limit we place on n. For the galaxies that were best fit with n = 6 in the original fits, these new fits yield residual-corrected sizes that are a median of 10% larger than those fit with n = 6, which is a significant change but is not one that would significantly alter any of our conclusions about the size of the sample relative to coeval galaxies. In addition, we also run a set of fits with an additional pointsource component fixed to the same centroid as the galaxy of interest. \sim 25% of these fits fail to converge, and among those that do converge, the majority are fit with an essentially negligible point-source component (median Sérsic mag point-source mag = -2.47). Additionally, the galaxies that are fit with significant with point-source components tend not to be those that are at the n = 6 boundary. We conclude that deviations from Sérsic profiles are likely being driven by PSF models that are not perfectly matched to the intrinsically high Sérsic index galaxies we are fitting. On the whole, all conclusions regarding the size of the galaxies are not strongly influenced by the inability to perfectly determine the Sérsic index, as evidenced by the very good match in the sizes of the LEGA-C quiescent galaxies we measure to those measured using HST/ACS imaging (see Appendix A).

The distribution of projected axis ratios for SQuIGG \vec{L} E post-starburst galaxies also skews significantly higher star-forming galaxies and slightly higher than quiescent galaxies. Taken together, these parametric measures indicate that post-starburst galaxies structurally appear to be fairly compact spheroids. If these galaxies began their lives as extended disks, any structural transformation must have predated or occurred concurrently with the shutdown of star formation, such that they structurally compact $\sim 100 \, \mathrm{Myr}$ after quenching.

4.3. Nonparametric Measures of Structure

Although we have shown that the light profiles of the poststarburst galaxies and the coeval control sample do not significantly deviate from Sérsic, the assumption of Sérsic profiles, especially those that run up against an artificial barrier in Sérsic index n, may introduce model dependent effects that muddy interpretations of compactness. Therefore, as a parallel test, we turn to nonparametric measures, namely the Gini coefficient and the generalized concentration (GC), which we measure using the GALMORPH suite (Freeman et al. 2017). We use the standard definition of the Gini coefficient defined in Abraham et al. (2003). However, the definition of the generalized concentration differs from the traditional concentration statistic (e.g., Conselice 2003) by not using circular apertures but instead by comparing the minimum number of pixels that contain 20% of the galaxy's light (a_{20}) to the minimum number of pixels containing 80% of the galaxy's

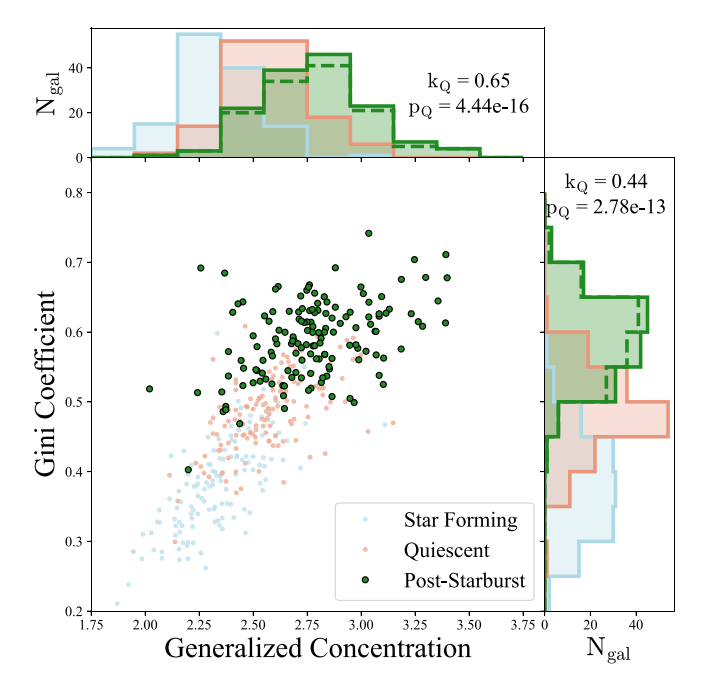


Figure 9. Gini coefficient vs. the generalized concentration for the mass-matched post-starburst (green), quiescent (red), and star-forming (blue) galaxies. The dashed post-starburst histogram shows the post-starburst galaxies that are mass-matched to the star-forming sample. These nonparametric measures of light concentration are strongly correlated. By both measures, the post-starburst population is more concentrated than both the quiescent and star-forming populations, in agreement with Sérsic parameters.

light (a_{80}) as follows:

$$GC = 5 \log_{10} \frac{a_{80}}{a_{20}}. (3)$$

These measures rely only on the rank ordering of pixels after source identification is performed. Higher values of these parameters indicate a high concentration of light in very few pixels.

In Figure 9, we show the distributions of the post-starburst and control samples in this space for the mass-matched samples. The two measures are indeed correlated, and confirm the compact nature of post-starburst galaxies relative to the quiescent and star-forming control samples. The post-starburst galaxies are particularly distinct from star-forming galaxies in Gini-concentration plane, indicating that if these galaxies are the descendants of similarly extended star-forming galaxies, they must have undergone a significant structural transformation. This is the same conclusion we draw from the parametric metrics (see Section 4.2).

5. The Origins of Compact Post-starburst Galaxy Structure

In this section, we speculate on the origin of the compact structure and identify possible progenitors to the rapid channel of quenching.

5.1. Testing the Central Starburst Scenario

Quenching caused by merger-driven central starbursts resulting in quenched galaxies have been shown to occur in simulations (e.g., Bekki et al. 2005; Wellons et al. 2015), and gas-rich wet compaction events could similarly cause a centrally concentrated starburst that, post-burst, would appear compact (Zolotov et al. 2015; Tacchella et al. 2016).

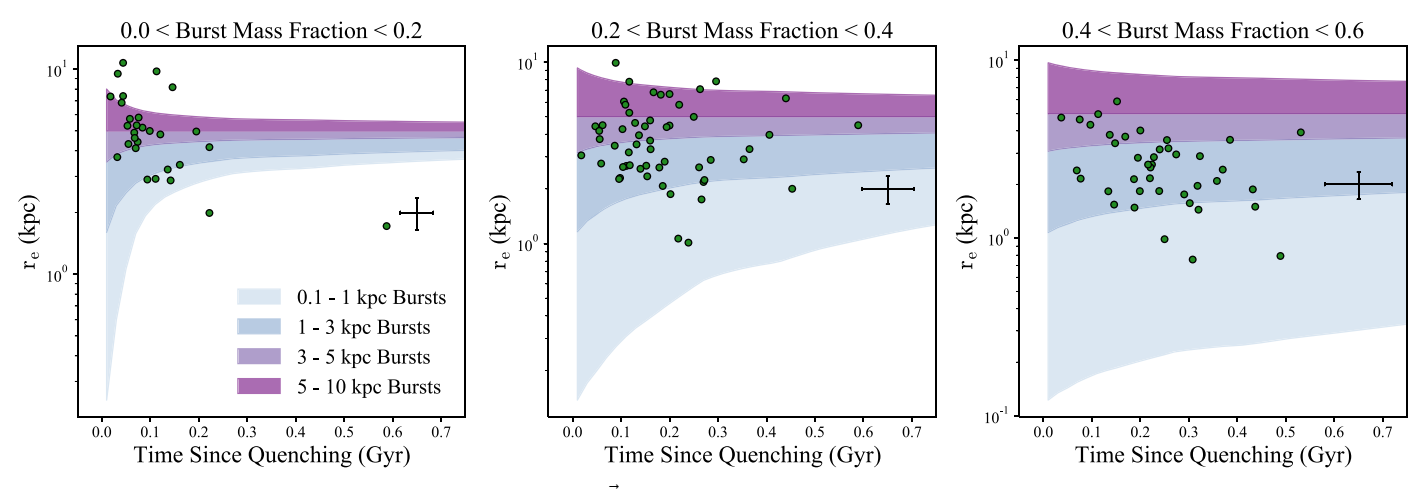


Figure 10. Half-light radius vs. time since quenching for the SQuIGG \vec{L} E post-starburst galaxies, divided into three bins of burst mass fraction (as measured in Suess et al. 2022). In the background, we shade the regions of size evolution populated by burst models described in Section 5.1 for a range of central burst sizes. We find that the majority of SQuIGG \vec{L} E post-starburst galaxies are inconsistent with the models of a subkiloparsec scale burst and can only be well-described by bursts that are extended on 1–10 kpc scales.

Observations of post-starburst galaxies have suggested that their compact structures are consistent with being the result of a recent central starburst (Wu et al. 2018, 2020; D'Eugenio et al. 2020b). In addition, at redshifts similar to those of SQuIGG \vec{L} E, extremely compact starburst galaxies have been observed with \sim 25% of the mass of $10^{11} M_{\odot}$ galaxies existing in the central \sim 100 pc (Sell et al. 2014; Diamond-Stanic et al. 2021).

Our previous study of six galaxies in the SQuIGG \vec{L} E sample using spatially resolved spectroscopy measured flat age gradients, disfavoring formation via a secondary central burst of star formation (Setton et al. 2020). However, if the recent burst of star formation totally dominates the light of the galaxy, hiding existing gradients, we would expect those signatures to fade with time. As the SQuIGG \vec{L} E sample spans a range of 0-700 Myr since quenching, we can use it to test whether galaxies are consistent with centralized starbursts imposed on older, more extended populations. Because the youngest, brightest stars in newly formed stellar populations die the most quickly, a central starburst's influence on the size of a galaxy would become weaker with time, leading to size growth as a function of the time since quenching. In Figure 10, we show a subset of the SQuIGG \vec{L} E sample divided up into bins of burst mass fraction (as measured in Suess et al. 2022) to show trends for galaxies which formed a similar fraction of their stellar mass in the recent burst of star formation. None of these bins show the predicted positive trend for a central starburst; conversely, the smallest and largest burst fraction bins are consistent with a negative slope (Spearman correlations for the 0%–20% bin: $\rho = -0.52$, p = 0.004; Spearman correlations for the 40%–60% bin: $\rho = -0.38$, p = 0.01), and the central bin is consistent with no slope (Spearman correlation for the 20%–40% bin: $\rho = -0.10, p = 0.45$). We additionally test for correlations between the Gini coefficient and the generalized concentration parameters and find no significant correlation with the time since quenching. The lack of a positive correlation between these measures of concentration and the time since quenching suggests that highly centralized star formation is unlikely to have occurred prior to quenching in post-starburst galaxies.

We further illustrate this result via the use of a toy model of half-light radius evolution. Using fsps (Conroy et al. 2009; Conroy & Gunn 2010; Foreman-Mackey et al. 2014) to track

the evolution of the rest-frame optical light with time, we simulate the superposition of an instantaneous burst of star formation on an older galaxy population by modeling both the galaxy and the burst as n = 4 Sérsic profiles. We fix the older population to be 1 Gyr old and to have $r_e = 5$ kpc, the approximate size of a $10^{11} M_{\odot}$ quiescent galaxy at this redshift. We test three burst regimes, 0%-20% burst fraction (modeled with a 10% burst), 20%-40% burst fraction (modeled with a 30% burst), and 40%–60% burst fraction (modeled with a 50% burst), and a range of burst geometries ranging from an extremely centralized 100 pc burst to an extended 10 kpc burst. We set the central and underlying dust attenuation to 0.5 and 0.1 dex respectively using the fsps dust2 parameter to reflect that the central region may be significantly more attenuated than the older population, but still restricting to the range of best-fitting dust values from spectrophotometric modeling (median dust2 \sim 0.3, see Suess et al. 2022). We note that these assumptions neglect the possibility that heavily obscured star formation is contained in the galaxies. Some post-starburst galaxies have been shown to contain deeply embedded dust reservoirs in the central ~ 100 pc with $A_v \sim 10^4$, which could in principle shield large amounts of central star formation (Smercina et al. 2022). However, in a previous study of CO(2–1) for a small (13 galaxies) subsample of SQuIGGLE, we do not see evidence of centrally concentrated molecular gas or continuum emission in the detected galaxies at $\sim 1''$ resolution. We measure molecular gas effective radii on the order of kiloparsecs and do not detect continuum emission in all but one galaxy (Bezanson et al. 2022). As such, we assume dust obscuration informed by our best fits to IR spectrophotometric data.

We show the tracks generated by these models as shaded regions on Figure 10. The vast majority of SQuIGG \vec{L} E galaxies are inconsistent with a subkiloparsec scale burst of star formation. To ensure that these conclusions are not heavily dependent on toy model assumptions about the underlying galaxy age and size, we test for a range of values ($r_e = 3$ kpc and 10 kpc, age = 0.5 Gyr) and find that the majority of galaxies are too large to ever overlap with the subkiloparsec burst tracks. We note that these observed kiloparsec-scale bursts of star formation do not completely eliminate mergers as a possible trigger for inducing the burst and subsequent

suppression of star formation, as integral field unit studies of post-merger galaxies have found evidence for centrally peaked but still global enhancements in star formation rate (Thorp et al. 2019). The lack of agreement between models for a highly concentrated burst of star formation and the size-age trends we observe only shows that star formation could not have occurred solely in the central regions of recently quenched galaxies.

The negative/inconclusive trends in r_e versus time since quenching indicate that these post-starburst galaxies do not evolve significantly in their \sim 500 Myr after quenching and that the youngest stars in the galaxy are distributed on spatial scales similar to any underlying older population. This is consistent with the finding that a small sample of SQuIGGLE poststarburst galaxies exhibit flat age gradients (Setton et al. 2020), which are also seen in young quiescent galaxies closer to cosmic noon (Akhshik et al. 2020; Jafariyazani et al. 2020) and compact local quiescent galaxies that may be the descendants of early universe rapid quenching (Schnorr-Müller et al. 2021). As we are still accounting for some unmasked tidal light in the fits to our galaxy sizes (see Figure 4), we propose that any negative trend in time since quenching versus size may be the result of tidal features that are commonly present in the young post-starburst galaxies (e.g., Sazonova et al. 2021; M. Verrico et al. 2022, in preparation) and that fade on \sim 200 Myr timescales. There is evidence for this when we split the sample into disturbed and nondisturbed using the classifications from M. Verrico et al. (2022, in preparation), as the youngest galaxies in the sample are far more likely than the oldest ones to host visible tidal features. However, we note that the sizes of the galaxies we fit are not being primarily driven by asymmetric non-Sérsic light, as the corrections for the disturbed and nondisturbed samples are both consistent with no systematic offset in measured half-light radius, and instead are primarily driven by the central light of the galaxy due to our aggressive deblending and masking.

Why, then, do the SQuIGG \vec{L} E post-starburst galaxies differ from other populations of post-starburst galaxies whether locally (Wu 2021) or at intermediate redshift (Wu et al. 2018; D'Eugenio et al. 2020b) that do show evidence of centrally concentrated star formation? The answer may lie in selection. High-mass galaxies in samples selected using $H_{\delta,A}$ equivalent width techniques like those in Wu et al. (2018) have been shown to have very small burst mass fractions, on the order of \sim 5% (French et al. 2018). The bursts in these galaxies are weak relative to the >20% bursts in SOuIGG \vec{L} E galaxies that are completely dominated by A-type populations (Suess et al. 2022). The galaxies with small bursts may represent a dusting of central star formation on top of an already quiescent population (which is similar to the toy model that does a poor job of describing SQuIGGLE post-starburst size evolution) rather than a true quenching of a galaxy's primary epoch of star formation that occurs in the entire galaxy simultaneously. High-redshift, massive post-starburst galaxies have been found to lack color gradients, suggesting that galaxies must shut off star formation such that a young stellar population dominates the light at all radii on kiloparsec scales in the immediate aftermath of quenching (Maltby et al. 2018; Suess et al. 2020). These fundamental differences in the galaxy masses, burst mass fractions, and stellar age distributions between low- and highredshift post-starburst galaxies may be the result of fundamentally different physical processes (e.g., increased major merger rates or higher gas fractions at earlier cosmic time). We suggest

that the SQuIGG \vec{L} E post-starburst galaxies are the lower-z extension of that population of rapidly quenching galaxies, and explore in the following section what progenitors could have resulted in the formation of compact post-starburst galaxies without purely central star formation.

5.2. Preferential Fast Quenching in Compact Star-forming Galaxies

The commonly invoked central starburst pathway to quiescence is often proposed as a way to take an extended star-forming galaxy and to produce a more concentrated elliptical galaxy. However, galaxies need not shrink down in the size–mass plane. Instead, these galaxies may have small sizes because they are the evolutionary descendants of more compact star-forming galaxies, which quenched rapidly after reaching a stellar density threshold that is correlated with other feedback mechanisms (e.g., van Dokkum et al. 2015).

In Figure 11(a) we show the relationship between the stellar mass and stellar surface mass density in the central kiloparsec for the galaxies in SOuIGG \vec{L} E and LEGA-C. Post-starburst galaxies are only slightly denser than the quiescent galaxies at this redshift (median log $(\Sigma_{1 \text{ kpc,PSB}}) - \log(\Sigma_{1 \text{ kpc},Q}) = 0.10$). In contrast, the post-starburst and quiescent samples are significantly more dense than star-forming galaxies at fixed stellar mass (median log ($\Sigma_{1 \text{ kpc,PSB}}$) – $\log(\Sigma_{1 \text{ kpc,SF}}) = 0.48$). The density of the post-starburst galaxies is similar to those found in previous studies of quiescent galaxies at this stellar mass, $\log(\Sigma_{1 \text{ kpc}}) \sim 10$ (e.g., Fang et al. 2013; van Dokkum et al. 2015; Barro et al. 2017; Mosleh et al. 2017; Whitaker et al. 2017; Suess et al. 2021). This supports the finding that galaxy structure in the central regions is largely set at the time quenching occurs. In addition, we find that dense central structures are in place for the entirety of the SQuIGGLE sample, regardless of the presence of tidal features; in Figure 11(b), we show that there is no significant difference in $\Sigma_{1 \text{ kpc}}$ between the disturbed and nondisturbed populations. This does not preclude mergers helping the galaxies reach the central density threshold required for shutdown; simulations that rely on AGN feedback to quench galaxies have shown that only mergers that push galaxies into the regime where their central black holes are massive enough to trigger feedback effectively quench galaxies (Quai et al. 2021), and more rapid quenching is strongly associated with an increased injection of AGN feedback prior to quenching (Park et al. 2021) However, it does suggest that mergers may not be the smoking-gun progenitor of all post-starburst galaxies.

Because the central mass of a galaxy and the black hole mass are strongly correlated (Kormendy & Ho 2013), it is natural to investigate the incidence of AGN in these dense post-starburst galaxies. The youngest galaxies in SQuIGG \vec{L} E host optical AGN at significantly higher rates than the oldest post-starburst galaxies and older quiescent galaxies (Greene et al. 2020). If feedback from AGN is connected to density, then it is possible that these galaxies went through a quasar phase that is still turning off in the youngest galaxies in the sample and that the galaxies will remain quenched after the AGN runs out of fuel and shuts down due to radio-mode feedback (e.g., Croton et al. 2006). After that, minor mergers will contribute to the growth in outer density to grow galaxies without substantially changing their central density (e.g., Bezanson et al. 2009; van Dokkum et al. 2010). This ex situ growth could lead to a better match in the half-light radii of the galaxies as they grow

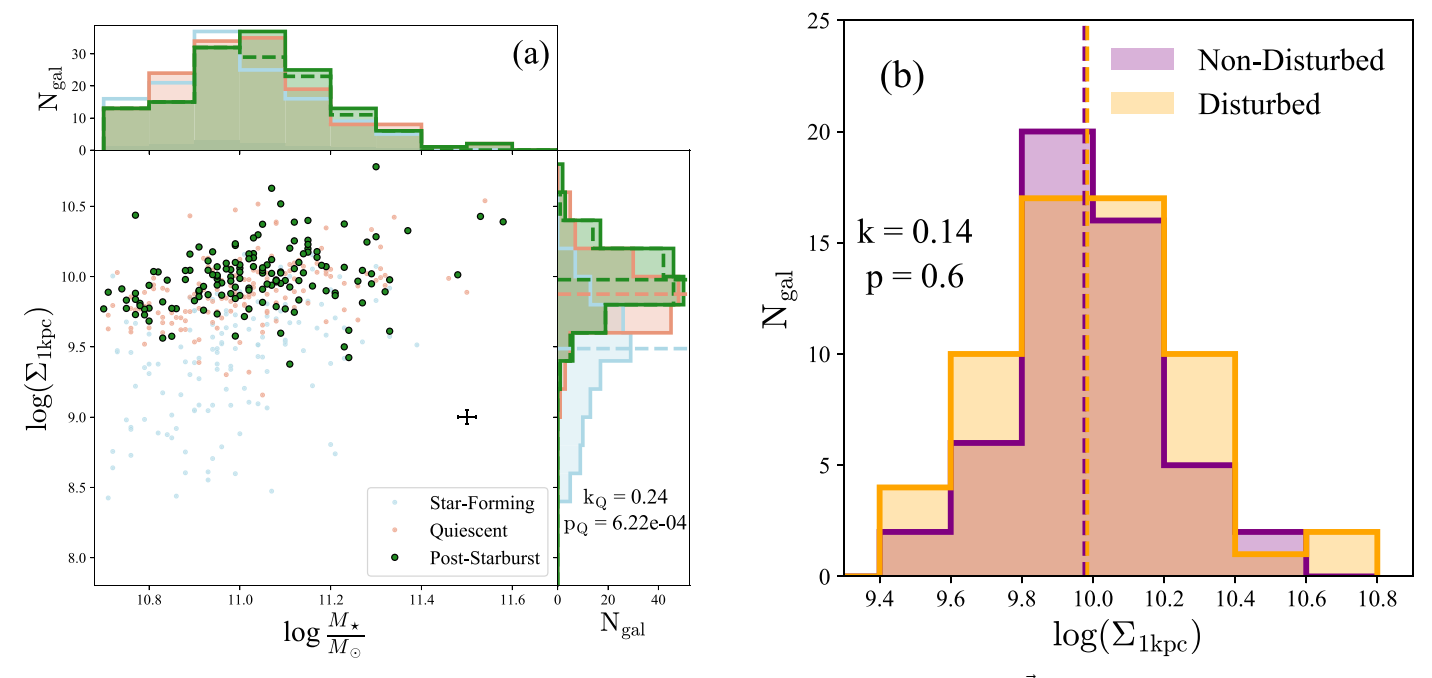


Figure 11. (Left) Stellar mass surface density in the central kiloparsec as a function of the stellar mass for SQuIGG \vec{L} E along with the star-forming and quiescent subsamples. Typical error bars derived from the PSF shuffling procedure are shown in black. The dashed post-starburst histogram shows the post-starburst galaxies that are mass-matched to the star-forming sample. SQuIGG \vec{L} E galaxies are only slightly denser than quiescent galaxies, while star-forming galaxies are significantly less dense than both populations. The results of a Kolmogorov–Smirnov test between the quiescent and post-starburst σ one distributions are shown on the vertical histogram. (Right) The distributions of in $\Sigma_{1 \text{ kpc}}$ for the disturbed and nondisturbed post-starburst populations, as defined in M. Verrico et al. (2022, in preparation). As with the compactness at fixed stellar mass (see Figure 7), a Kolmogorov–Smirnov test shows that the distributions are not significantly different between the two populations. The SQuIGG \vec{L} E sample of post-starburst galaxies is uniformly dense in its core regions.

their sizes without significantly changing their central structures.

The similar central densities and discrepant half-light radii of post-starburst and quiescent galaxies implies that the profiles should differ in shape most significantly in the wings if ex situ growth is the dominant mode of evolution post-quenching. To investigate this, we derive 1D surface mass profiles for the post-starburst and quiescent galaxies by multiplying the observed surface brightness profiles by the mass-to-light ratio, assuming no radial gradients. In Figure 12, we show the median surface mass profiles for the post-starburst and quiescent samples with associated scatter, as well as the difference between the median profiles. The ex situ growth hypothesis is supported by these stellar-mass profiles, as the differences between the median profiles increases steadily out to a = 10 kpc. This profile difference at large radii is likely less extreme in reality due to the empirical color gradients found in quiescent galaxies (e.g., Suess et al. 2019a, 2019b, 2020; Kawinwanichakij et al. 2021). Quiescent galaxies tend to be bluer in their outskirts, which would lead to a smaller mass-tolight ratio and would alleviate at least some of the tension between these profile shapes. However, the color gradients present in quiescent samples are likely the result of the minor mergers we suggest are the dominant growth path postquenching, and this normalization scheme still shows that the shapes of the profiles are most significantly different at a > 10 kpc. Taken together, we suggest that in rapid quenching, the seeds of the structure of the quiescent population are formed in the recent burst on kiloparsec scales, after which feedback correlated with density suppresses any additional star formation and minor mergers become the primary form of galaxy mass growth.

One possible class of progenitors could be dusty, extreme starbursts, or "submillimeter galaxies" (Toft et al. 2012, 2014; Wild et al. 2020), which have the extremely high star formation rates and feedback necessary to produce galaxies like those in SQuIGGLE (Spilker et al. 2020a, 2020b). At high redshift, submillimeter galaxies also lie slightly below quiescent galaxies in the mass-size plane (Gómez-Guijarro et al. 2022). If they shut off their rapid star formation abruptly and uniformly, submillimeter galaxies would likely result in poststarburst SEDs and flat age gradients similar to those measured in SQuIGGLE galaxies (Setton et al. 2020). While detailed analysis of number densities is beyond the scope of this work, we note that in LEGA-C, star-forming galaxies do exist that are dense enough in $\log(\Sigma_{1 \text{ kpc}})$ to evolve into SQuIGGLE poststarburst galaxies without a significant amount of additional compaction. These galaxies do not have star formation rates high enough to be submillimeter galaxies, but it is unlikely that such extremely rare progenitors would be found in a field as small as that of LEGA-C. Future work will focus on more strongly constraining the density of SQuIGGLE-like poststarburst galaxies as a function of redshift to tie them more concretely to a progenitor population.

Ultimately, we conclude that the recent star formation in post-starburst galaxies must have taken place on spatial scales that are comparable to the size of the galaxy, as we do not see any evidence of the type of fading that would be expected from a centralized starburst. Although galaxy mergers likely play a role in quenching some of the post-starburst galaxies in SQuIGGLE (see M. Verrico et al. 2022, in preparation), the finding that $\log(\Sigma_{1\,\mathrm{kpc}})$ is fully consistent between the disturbed and nondisturbed samples and the lack of positive size evolution suggests that merger-driven central starbursts are

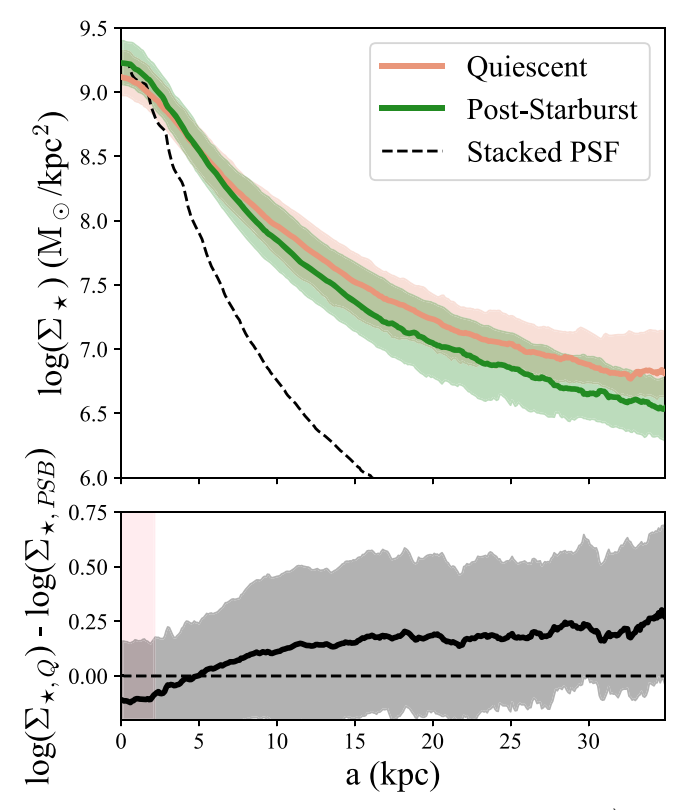


Figure 12. 1D median stacks of the surface mass profiles of SQuIGG \vec{L} E post-starburst galaxies (green) and the mass-matched LEGA-C control sample (red) as a function of the semimajor axis of the best-fitting ellipse in kiloparsecs. The profiles are truncated at the radius where the number of galaxies used in the stack drops below 20. Also shown is a stack of the model point-spread functions used in the fits (black dashed line). The bands bound the 16th and 84th percentile surface mass profiles for each sample. In the bottom panel, we show the difference between the quiescent and post-starburst median profiles as a black line with combined scatter indicated as a gray band, with the half width at half maximum seeing $(0.\%3 \sim 2.1 \text{ kpc}$ at z = 0.7) indicated by the pink shaded region. The differences in the profiles increases as a function of the radius, flattening at $\sim 10 \text{ kpc}$.

not the entire story. Instead, the mergers may, in some galaxies, simply be the last push toward a central density high enough to trigger feedback that rapidly shuts off star formation while locking in existing structure and maintains the shutdown. After this, galaxies could passively evolve into red, quiescent galaxies that grow in half-light size via minor mergers but otherwise do not significantly change in their structures.

6. Conclusions

Using images from the HSC survey, we study the sizes and structures of $z \sim 0.7$ post-starburst galaxies from the SQuIGGLE survey (Suess et al. 2022) in comparison to coeval massive galaxies in the LEGA-C Survey. By performing single-component Sérsic fitting of the galaxies, we have robustly measured sizes that account for non-Sérsic low-surface-brightness features and structural measures like the Sérsic index and the axis ratio. In addition, we measure nonparametric indicators of concentration. We conclude the following:

1. Post-starburst galaxies have smaller half-light radii than coeval star-forming and quiescent galaxies at similar stellar mass (see Figures 6 and 7). Specifically, they are systematically ∼0.1 dex smaller than quiescent galaxies

- and \sim 0.4 dex smaller than star-forming galaxies. The compactness at fixed stellar mass does not vary strongly based on whether or not a galaxy is tidally disturbed.
- 2. The sizes and structures of post-starburst galaxies, as measured via parametric (see Figure 8) or nonparametric measures (see Figure 9) also point to concentrated, round galaxies that are more similar to quiescent galaxies than they are to star-forming galaxies.
- 3. Post-starburst galaxies either negative or flat correlation between their sizes and their time since quenching (see Figure 10). This trend stands in contrast with what would be expected for a fading central starburst, indicating that the recent burst of star formation was not limited to the galaxy center, and instead must have occurred on larger (≳1 kpc) spatial scales.
- 4. The central densities of post-starburst galaxies are very similar to those of quiescent galaxies (see Figure 11) and match the common threshold for quiescence, $\log(\Sigma_{1 \text{ kpc}})$ $\sim \! 10$ found in the literature.
- 5. The median shape of the post-starburst and quiescent surface brightness profiles are most significantly different at large radii ($a > 10 \,\mathrm{kpc}$), where the quiescent sample has more light (see Figure 12). This indicates that while the central shapes of galaxies do not change significantly once quiescence is reached, the outer envelopes may indeed grow via minor merging, which deposits stellar mass at large radii.

Two competing forces are at play in the detailed study of the rapid mode of quenching. On the one hand, fast quenching dominates at high redshift, so in the ideal case one would hunt for post-starburst galaxies at the highest redshift possible in order to identify candidates for galaxies that have recently shut off their primary epoch of star formation. On the other hand, in order to push to high redshift, deep integration times are required, which makes it difficult to cover the large patches of sky necessary to identify galaxies in this short-lived period of evolution. The ideal situation (deep, red spectroscopic surveys of large areas of the sky), however, is right around the corner with the impending public releases of deep spectroscopic surveys like the Dark Energy Spectroscopic Instrument (DESI Collaboration et al. 2016) and the Prime Focus Spectrograph (Takada et al. 2014) surveys. In the very near future, the high-quality spectra from these surveys will allow for the identification of large samples of post-starburst galaxies out past $z \sim 1$. Future studies of the galaxies identified in these surveys will significantly bolster our understanding of the rapid mode of quenching by identifying the first statistically large samples of post-starburst galaxies near the era of cosmic noon. The quantification of the number density, size, structure, AGN activity, and gas content of post-starburst galaxies as a function of redshift will place strong constraints on the rapid quenching pathway of galaxy evolution.

D.J.S., J.E.G., R.B., and D.N. gratefully acknowledge support from NSF grant AST1907723. This work was performed in part at the Aspen Center for Physics, which is supported by National Science Foundation grant PHY-1607611. D.J.S. would also like to thank the North American ALMA Science center for financial support in attending the ACP "Quenching" conference. M.V. acknowledges support from the NASA Pennsylvania Space Grant Consortium. R.F. acknowledges financial support from the Swiss National

Science Foundation (grant No. 157591 and 194814). D.J.S. thanks Alan Pearl, Brett Andrews, Yasha Kaushal, and Alwin Mao for their help with visual classifications as well as in perfecting color maps and point sizes down to the minutia. Finally, D.J.S. thanks Stephanie Permut for her kindness in listening to ramblings about "intermediate-redshift post-starburst galaxies" for months on end.

The Hyper Suprime-Cam (HSC) collaboration includes the astronomical communities of Japan and Taiwan, and Princeton University. The HSC instrumentation and software were developed by the National Astronomical Observatory of Japan (NAOJ), the Kavli Institute for the Physics and Mathematics of the Universe (Kavli IPMU), the University of Tokyo, the High Energy Accelerator Research Organization (KEK), the Academia Sinica Institute for Astronomy and Astrophysics in Taiwan (ASIAA), and Princeton University.

Funding for SDSS-III has been provided by the Alfred P. Sloan Foundation, the Participating Institutions, the National Science Foundation, and the U.S. Department of Energy Office of Science. The SDSS-III website is http://www.sdss3.org/.

SDSS-III is managed by the Astrophysical Research Consortium for the Participating Institutions of the SDSS-III Collaboration including the University of Arizona, the Brazilian Participation Group, Brookhaven National Laboratory, Carnegie Mellon University, University of Florida, the French Participation Group, the German Participation Group, Harvard University, the Instituto de Astrofisica de Canarias, the Michigan State/Notre Dame/JINA Participation Group, Johns Hopkins University, Lawrence Berkeley National Laboratory, Max Planck Institute for Astrophysics, Max Planck Institute for Extraterrestrial Physics, New Mexico State University, New York University, Ohio State University, Pennsylvania State University, University of Portsmouth, Princeton University, the Spanish Participation Group, University of Tokyo, University

of Utah, Vanderbilt University, University of Virginia, University of Washington, and Yale University.

Appendix A Verifying the Accuracy of Structural Measurements Using Ground-based Imaging

The i-band galaxy images from the HSC survey are remarkable both for their depths and resolutions from the ground, but their resolution (PSF FWHM ~ 0.16) is still dwarfed by that of space-based instruments like the HST (PSF FWHM ~ 0.115). We have turned to the HSC survey because obtaining space-based images of the entire SQuIGG \vec{L} E poststarburst sample is unfeasible; the galaxies are distributed throughout the entire SDSS footprint and it would require a significant investment to get HST follow-up imaging of the entire sample. However, the LEGA-C survey, which we utilize as a coeval comparison sample of galaxies, completely overlaps with HSC and also has existing HST/ACS F814 imaging. This means that we can directly compare the Sérsic sizes and structures we derive for LEGA-C galaxies to those measured in van der Wel et al. (2021) to test how our ground-based measurements compare to those from space.

In Figures 13 and 14, we show the comparisons between our measured sizes and Sérsic indices and the values measured from the HST images, split into quiescent (red) and star-forming (blue) populations. For the majority of galaxies, the sizes are fairly well recovered, especially in the quiescent populations where the percent error in the sizes scatters around 0%. However, for star-forming galaxies, there is a systematic offset, where the galaxies are measured in HST to be a median of \sim 8% larger than they are in HSC imaging. This difference is reflected in the Sérsic indices as well; quiescent populations are measured in HST with slightly higher Sérsic indices, but the difference is more pronounced in the star-forming populations.

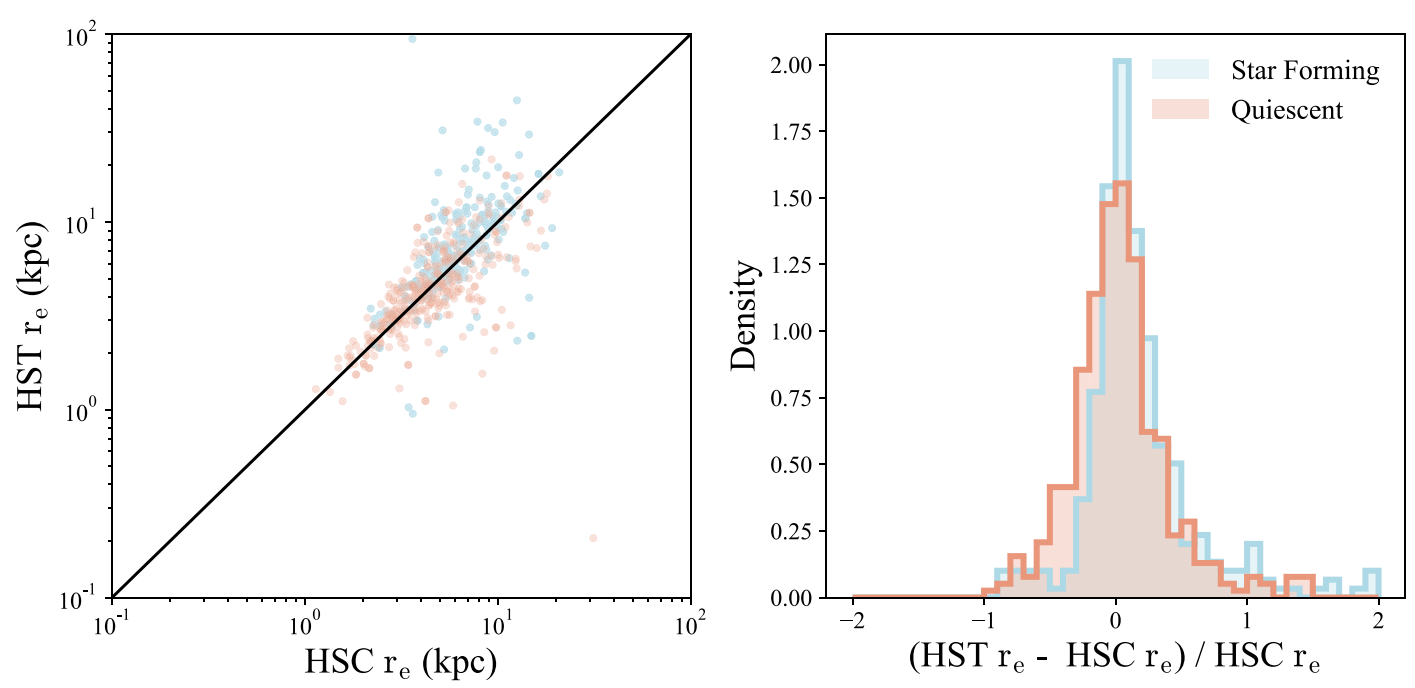


Figure 13. (Left) One-to-one relation between the Sérsic effective radii we measure on the HSC images and the Sérsic radii from van der Wel et al. (2021) measured from HST/ACS images. Star-forming galaxies are colored as blue, and quiescent galaxies are red. (Right) The percent difference in the measurements for the two LEGA-C samples. For quiescent galaxies, the median sizes we measure are extremely close, with a scatter of \sim 20%. For star-forming galaxies, the scatter is similar, but there is a systematic offset where the HST sizes are \sim 8% larger than the ones we measure. Both subsamples have longer tails in the direction of larger HST sizes.

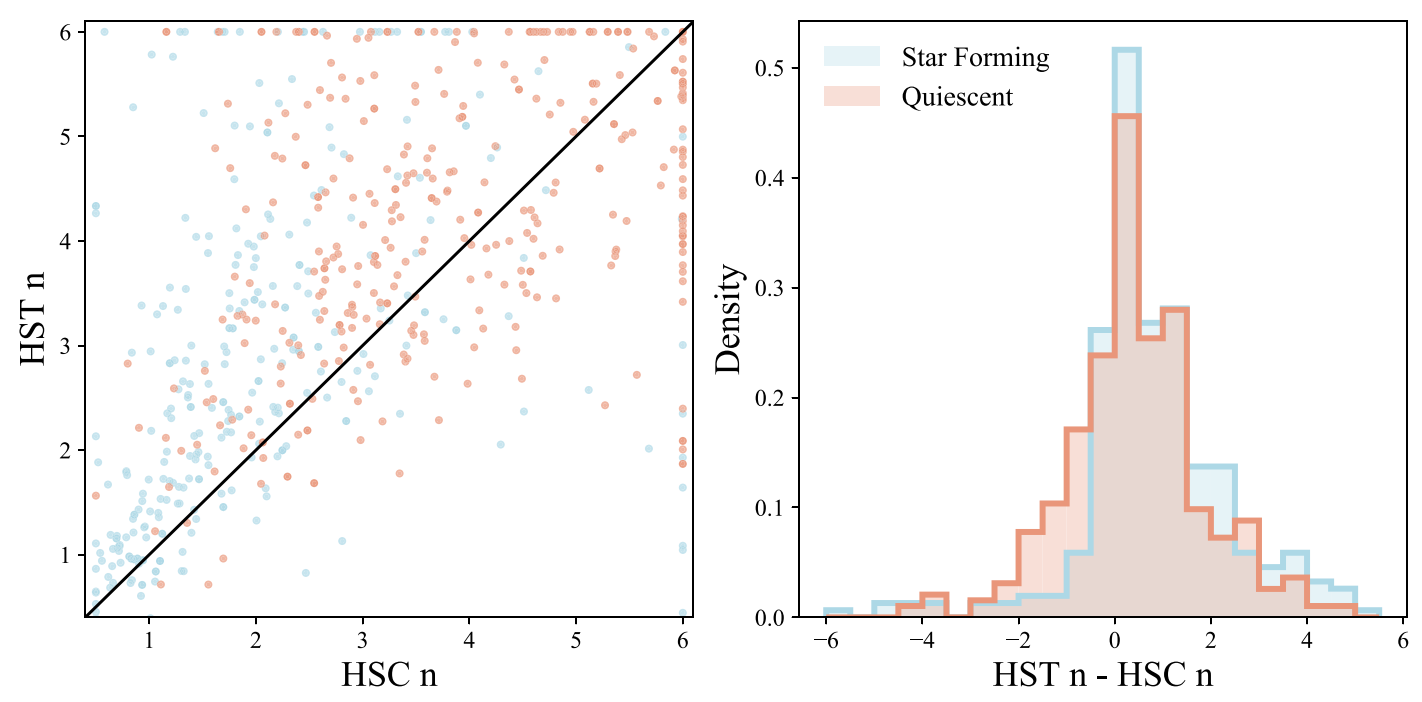


Figure 14. As in Figure 13, but for the Sérsic indices. In both the quiescent and star-forming subsamples, the Sérsic indices measured in the HST tend to be larger than those we measure with HST, but the trend is more pronounced for the star-forming galaxies.

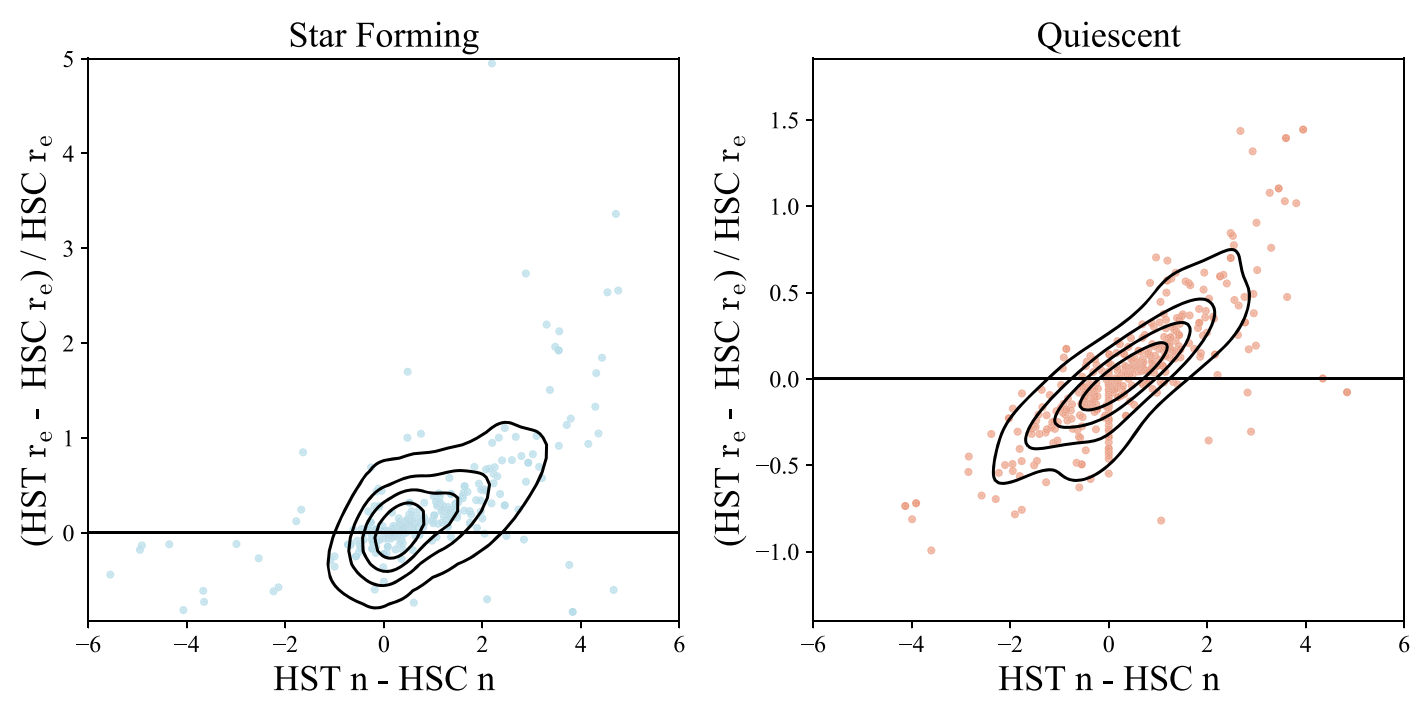


Figure 15. Percent difference in the size vs. the difference in Sérsic index for the star-forming (left) and quiescent (right) subsamples, with contours bounding 80% of the galaxies. There is a trend in both samples where a mismatch in Sérsic index correlates with a mismatch in the measured sizes. (Note: We truncate the y-axis on the star-forming plot at 5 despite a single point at \sim 25 due to a nonphysical HST measurement of that galaxy.)

In Figure 15, we show the covariance between these two offsets. Galaxies that are fit in the HST with larger sizes are also fit with larger Sérsic indices, and this tail at the larger-size/higher-Sérsic-index end is more pronounced in the star-forming population. Because a high Sérsic index corresponds to both a more peaked core and more extended wings, we turn to 1D surface brightness profiles to understand what is driving this difference. In order to do so, we generate models of the best-

fitting space-based galaxy parameters from van der Wel et al. (2021) at the pixel scale of HSC and convolved with the same HSC PSF we use to fit the galaxies. In order to avoid systematic differences in source identification and deblending, we restrict this test to galaxies that do not have a bright neighbor within 25 pixels. In Figures 16 and 17, we show residuals in the surface brightness profiles for galaxies as fit in this work (dark blue) and with the best-fitting models fit to the

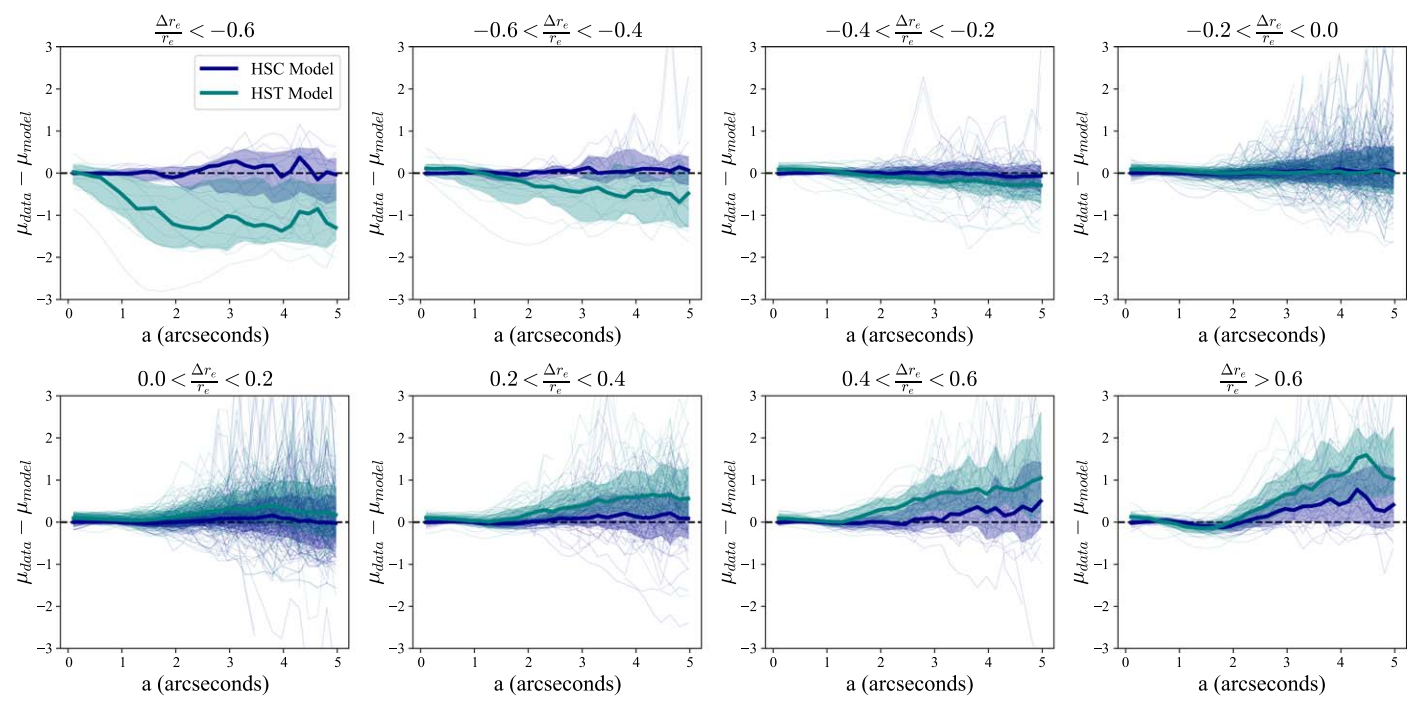


Figure 16. Individual (thin lines) and median (thick lines) residuals between the surface brightness profiles extracted from the cutouts and the best-fitting models from this work (dark blue) and the fits to HST ACS images described in van der Wel et al. (2016) convolved with the HSC PSF (teal). Separate panels show the galaxies binned by the agreement between the two fits in the effective radius. Profiles are only shown for galaxies where no nearby objects are simultaneously fit. In all cases, our model surface brightness profiles are consistent with no residuals. However, the HST fits that overestimate the sizes do so because they have significantly more light in the wings than our galaxies, as well as slightly more peaked cores.

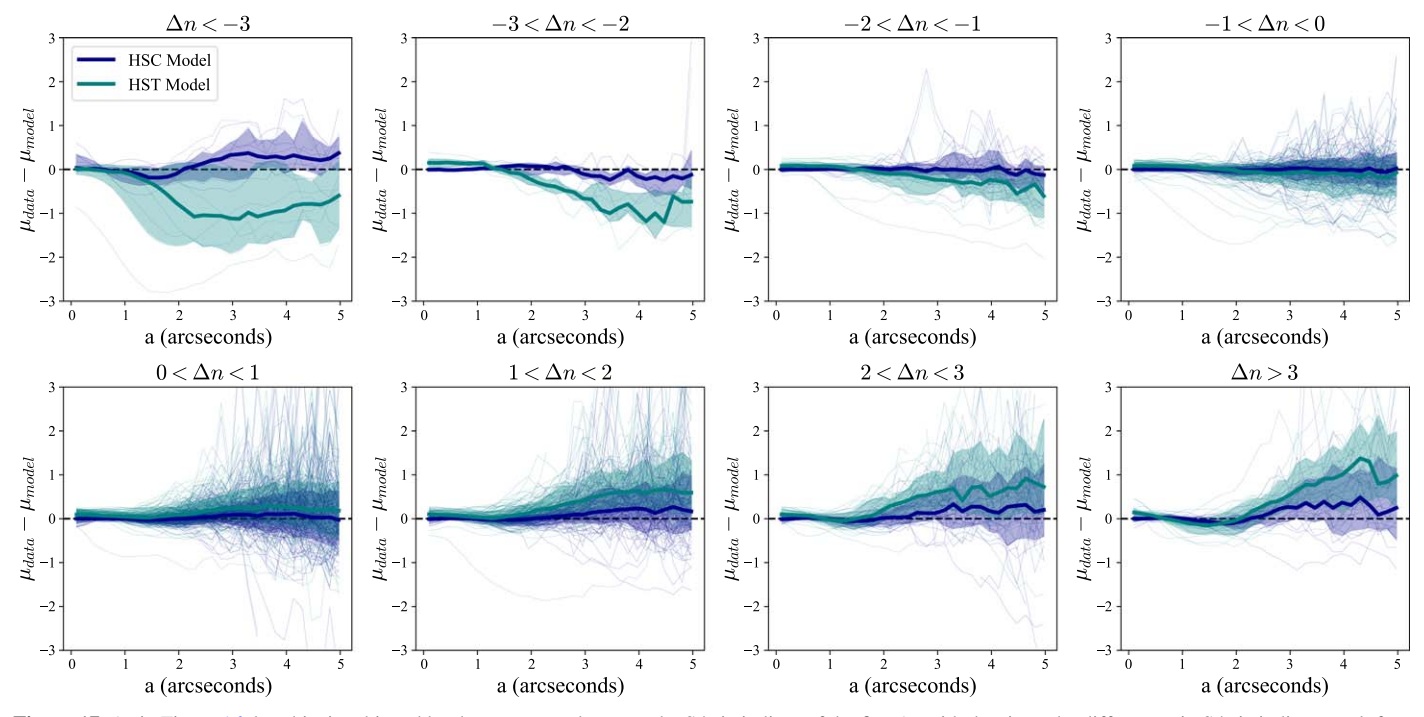


Figure 17. As in Figure 16, but this time binned by the agreement between the Sérsic indices of the fits. As with the sizes, the differences in Sérsic indices result from significant failures to successfully fit the low-surface-brightness wings in the HST images.

HST images of the galaxies under HSC viewing conditions (teal), binned by the offset between the two measurements. We find that the differences in size and Sérsic index are largely driven by a difference in the wings. The HST Sérsic structures

overpredict the amount of light that will be present at large radii, and, as a result, measure larger sizes. This is likely due to the sensitivity of HST to the cores of the galaxies; in trying to accurately fit the peaky centers of the galaxies, the HST fits

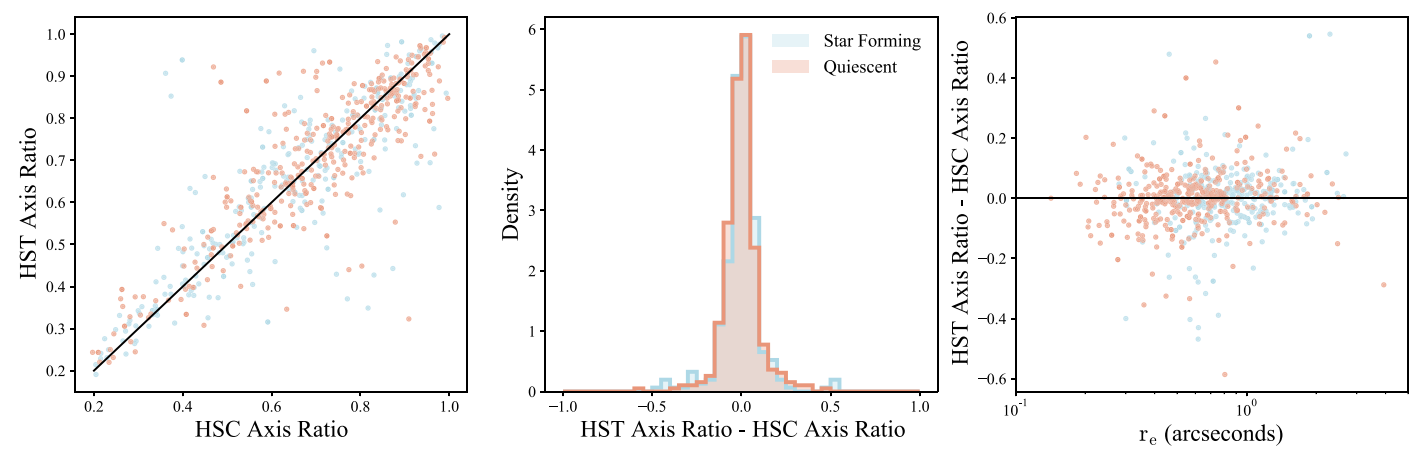


Figure 18. (Right) The axis ratio we measure using HSC data for quiescent (red) and star-forming (blue) LEGA-C galaxies vs. the same parameter measured using HST data. A 1:1 correspondence is shown in black. (Center) The difference in the measurements of the axis ratios. The median deviation is consistent with zero and the scatter is very small. (Right) Difference between the axis ratios as a function of the size in arcseconds. The smallest galaxies are as well recovered as the largest ones, indicating that even the smallest galaxies in $SQuIGG\vec{L}E$ that are resolved have axis ratio measurements that can be trusted.

converge to large n, which is compensated for by inflated sky values. In contrast, HSC's remarkable low-surface brightness limits (\sim 28.5 mag arcsec⁻²) allows for well-calibrated sky measurements that result in small residuals at large radii. This better allows for the galaxies to be fit with low Sérsic indices, which is more significant in the star-forming galaxies that tend to be more disk-like.

Our fitting does an especially good job at recovering the shapes of galaxies in their axis ratios. We illustrate this in Figure 18, showing the 1:1 relation between the projected axis ratios we measure and those from van der Wel et al. (2016). The values agree between the ground- and space-based measurements with a scatter of only ~0.07, indicating that even with significantly more PSF smearing, the projected galaxy shapes are still recoverable using GALFIT. Perhaps more important, there does not appear to be any trend with the sizes of the galaxies; in the right panel of Figure 18, we show that the difference in axis ratios does not correlate with the size for either the star-forming or quiescent control samples. Even at the low size ($r_e \sim 0.11$) limit where the sizes of the galaxies are significantly smaller than the PSF, the axis ratios are still robustly recovered. This indicates that the roundness that we measure in SQuIGG \vec{L} E galaxies is not just a resolution effect, but a real physical property we can trust in our interpretations.

We conclude that ground-based imaging with low-surface-brightness limits is extremely well suited for the task of measuring galaxies sizes and Sérsic structures. While the loss in resolution from the HST to the HSC does not allow for the centers of galaxies to be resolved, the increase in sensitivity at large radii allows for the total light of the galaxy to be better accounted for, which improves the measurement of $r_{\rm e}$. In addition, we find that observing from the ground does not affect measurements of the axis ratio significantly, even for the smallest galaxies.

Appendix B Comparing the Smallest Galaxies to an Unresolved Point Source

Despite the agreement between the sizes fit on the LEGA-C control sample and those in the HST, resolution is still a concern. The smallest galaxies in the SQuIGGLE sample are fit with sizes ~ 0.1 , whereas the median seeing in the HSC *i* band is $\sim 0.$ ''6. In order to confirm that all the sizes we report for galaxies are reliable from a ground-based survey, we rerun all our fits using an identical algorithm to the one outlined in Section 3.1, but this time we force the 2D galaxy profiles to be a point source convolved with the PSF we provide to GALFIT from the HSC PSF Picker. We calculate radial χ^2 values both the Sérsic and PSF-only models out to the point where the signal-to-noise ratio in the galaxy profile drops below 5, and find that the PSF-only models have median χ^2 values ~ 2.5 orders of magnitude higher than for the Sérsic models convolved with the PSF, indicating that the SQuIGG \vec{L} E sample is significantly resolved. Even the best performing PSF models are still significantly worse fits than Sérsic profiles.

To illustrate this, in Figure 19 we show the two smallest galaxies in SQuIGG \vec{L} E that do not have bright nearby companions, as well as the 2D and 1D best-fitting Sérsic and point-source models. The 1D profiles are extracted using the best-fitting axis ratio from the Sérsic model. It is clear from the residuals and the 1D profile that the Sérsic model better captures the true shape of the galaxy profiles, both in the centers (where the PSF is far too peaked) and in the wings. In addition, in the case of J2241+0025, there is a clear elongation in the galaxy that that the PSF shape cannot account for. Thus, even though the galaxy sizes we fit are small, we still consider them to be reliable when the PSF is properly accounted for in the fits.

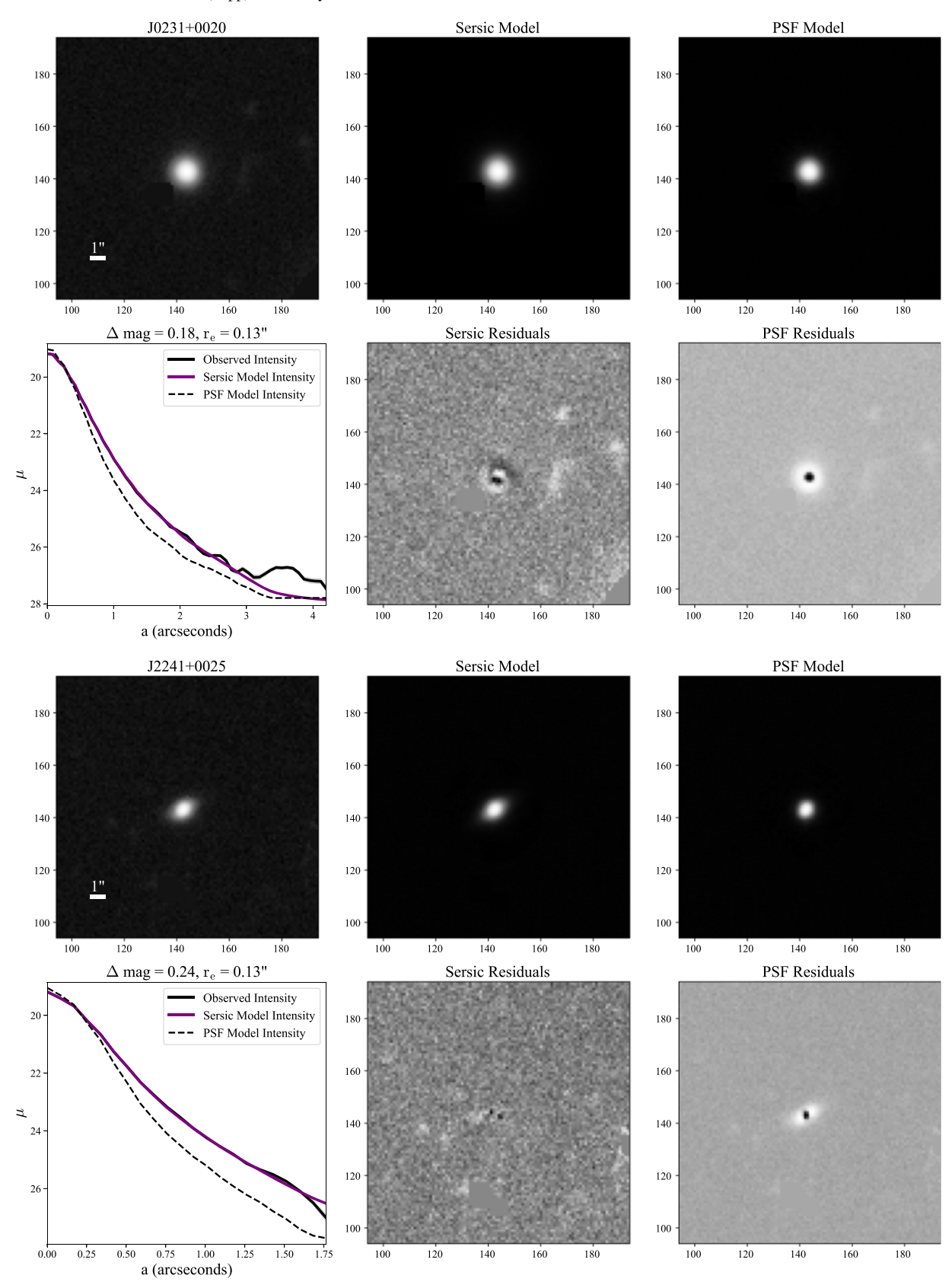


Figure 19. In the top row, $\sim 17'' \times 17''$ cutouts of the image (left), best-fitting Sérsic model (center), and best-fitting point-source model (right) generated with GALFIT for the two smallest galaxies in SQuIGG \vec{L} E with no neighbors that required simultaneous fitting. Below each of the models, we show the residuals, with masked pixels grayed out. In the bottom left, we show the 1D surface brightness profiles for the data (blue), the Sérsic model (red), and the point source (black). Profiles are truncated when the signal-to-noise ratio drops below 3. It is clear that even for $r_e \sim 0''_{..}$ 1 galaxies, the best-fitting point-source model will result in a galaxy that is too centrally peaked and that does not properly capture the galaxy wings seen in the data.

ORCID iDs

```
References
Abolfathi, B., Aguado, D. S., Aguilar, G., et al. 2018, ApJS, 235, 42
Abraham, R. G., van den Bergh, S., & Nair, P. 2003, ApJ, 588, 218
Aihara, H., AlSayyad, Y., Ando, M., et al. 2022, PASJ, 74, 247
Aihara, H., Arimoto, N., Armstrong, R., et al. 2018, PASJ, 70, S4
Akhshik, M., Whitaker, K. E., Brammer, G., et al. 2020, arXiv:2008.02276
Almaini, O., Wild, V., Maltby, D. T., et al. 2017, MNRAS, 472, 1401
Astropy Collaboration, Price-Whelan, A. M., Sipőcz, B. M., et al. 2018, AJ,
Astropy Collaboration, Robitaille, T. P., Tollerud, E. J., et al. 2013, A&A,
   558, A33
Barro, G., Faber, S. M., Koo, D. C., et al. 2017, ApJ, 840, 47
Bekki, K., Couch, W. J., Shioya, Y., & Vazdekis, A. 2005, MNRAS, 359, 949
Belli, S., Newman, A. B., & Ellis, R. S. 2019, ApJ, 874, 17
Bezanson, R., Spilker, J. S., Suess, K. A., et al. 2022, ApJ, 925, 153
Bezanson, R., van Dokkum, P. G., Tal, T., et al. 2009, ApJ, 697, 1290
Bosch, J., Armstrong, R., Bickerton, S., et al. 2018, PASJ, 70, S5
Bruzual, G., & Charlot, S. 2003, MNRAS, 344, 1000
Calzetti, D. 1997, AJ, 113, 162
Chabrier, G. 2003, PASP, 115, 763
Chen, Y.-M., Shi, Y., Wild, V., et al. 2019, MNRAS, 489, 5709
Conroy, C., & Gunn, J. E. 2010, ApJ, 712, 833
Conroy, C., Gunn, J. E., & White, M. 2009, ApJ, 699, 486
Conselice, C. J. 2003, ApJS, 147, 1
Croton, D. J., Springel, V., White, S. D. M., et al. 2006, MNRAS, 365, 11
Davidzon, I., Ilbert, O., Laigle, C., et al. 2017, A&A, 605, A70
Dawson, K. S., Schlegel, D. J., Ahn, C. P., et al. 2013, AJ, 145, 10
DESI Collaboration, Aghamousa, A., & Aguilar, J. 2016, arXiv:1611.00036
D'Eugenio, C., Daddi, E., Gobat, R., et al. 2020a, ApJL, 892, L2
D'Eugenio, F., van der Wel, A., Wu, P.-F., et al. 2020b, MNRAS, 497, 389
Diamond-Stanic, A. M., Moustakas, J., Sell, P. H., et al. 2021, ApJ, 912, 11
Dressler, A., & Gunn, J. E. 1983, ApJ, 270, 7
Fang, J. J., Faber, S. M., Koo, D. C., & Dekel, A. 2013, ApJ, 776, 63
Fasano, G., & Franceschini, A. 1987, MNRAS, 225, 155
Foreman-Mackey, D., Hogg, D. W., Lang, D., & Goodman, J. 2013, PASP,
   125, 306
Foreman-Mackey, D., Sick, J., & Johnson, B. 2014, python-fsps: Python
   Bindings to FSPS, v0.1.1, Zenodo, doi:10.5281/zenodo.12157
Forrest, B., Marsan, Z. C., Annunziatella, M., et al. 2020, ApJ, 903, 47
Freeman, P. E., Kim, I., & Lee, A. B. 2017, MNRAS, 471, 3273
French, K. D. 2021, PASP, 133, 072001
French, K. D., Yang, Y., Zabludoff, A., et al. 2015, ApJ, 801, 1
French, K. D., Yang, Y., Zabludoff, A. I., & Tremonti, C. A. 2018, ApJ, 862, 2
Gómez-Guijarro, C., Elbaz, D., Xiao, M., et al. 2022, A&A, 658, A43
Greene, J. E., Setton, D., Bezanson, R., et al. 2020, ApJL, 899, L9
Jafariyazani, M., Newman, A. B., Mobasher, B., et al. 2020, ApJL, 897, L42
Johnson, B., Foreman-Mackey, D., Sick, J., et al. 2021, dfm/python-fsps:
   python-fsps, v0.4.0, Zenodo, doi:10.5281/zenodo.4577191
Johnson, B., & Leja, J. 2017, Bd-J/Prospector: Initial Release, v0.1, Zenodo,
   doi:10.5281/zenodo.1116491
Kalita, B. S., Daddi, E., D'Eugenio, C., et al. 2021, ApJL, 917, L17
Kawanomoto, S., Uraguchi, F., Komiyama, Y., et al. 2018, PASJ, 70, 66
Kawinwanichakij, L., Silverman, J. D., Ding, X., et al. 2021, ApJ, 921, 38
Kormendy, J., & Ho, L. C. 2013, ARA&A, 51, 511
Kriek, M., Labbé, I., Conroy, C., et al. 2010, ApJL, 722, L64
Kriek, M., van Dokkum, P. G., Labbé, I., et al. 2009, ApJ, 700, 221
```

```
Leja, J., Johnson, B. D., Conroy, C., van Dokkum, P. G., & Byler, N. 2017,
    ApJ, 837, 170
Leja, J., Speagle, J. S., Ting, Y.-S., et al. 2021, arXiv:2110.04314
Lower, S., Narayanan, D., Leja, J., et al. 2020, ApJ, 904, 33
Maltby, D. T., Almaini, O., Wild, V., et al. 2018, MNRAS, 480, 381
Matharu, J., Muzzin, A., Brammer, G. B., et al. 2020, MNRAS, 493, 6011
Matharu, J., Muzzin, A., Brammer, G. B., et al. 2021, ApJ, 923, 222
McLeod, D. J., McLure, R. J., Dunlop, J. S., et al. 2021, MNRAS, 503, 4413
Mosleh, M., Tacchella, S., Renzini, A., et al. 2017, ApJ, 837, 2
Mowla, L. A., van Dokkum, P., Brammer, G. B., et al. 2019, ApJ, 880, 57
Muzzin, A., Marchesini, D., Stefanon, M., et al. 2013, ApJ, 777, 18
Park, M., Tacchella, S., Nelson, E. J., et al. 2021, arXiv:2112.07679
Pathak, D., Belli, S., & Weinberger, R. 2021, ApJL, 916, L23
Pattarakijwanich, P., Strauss, M. A., Ho, S., & Ross, N. P. 2016, ApJ, 833, 19
Pawlik, M. M., Wild, V., Walcher, C. J., et al. 2016, MNRAS, 456, 3032
Peacock, J. A. 1983, MNRAS, 202, 615
Peng, C. Y., Ho, L. C., Impey, C. D., & Rix, H.-W. 2010, AJ, 139, 2097
Pracy, M. B., Couch, W. J., Blake, C., et al. 2005, MNRAS, 359, 1421
Quai, S., Hani, M. H., Ellison, S. L., Patton, D. R., & Woo, J. 2021, MNRAS,
Sazonova, E., Alatalo, K., Rowlands, K., et al. 2021, ApJ, 919, 134
Schaye, J., Crain, R. A., Bower, R. G., et al. 2015, MNRAS, 446, 521
Schnorr-Müller, A., Trevisan, M., Riffel, R., et al. 2021, arXiv:2104.12737
Sell, P. H., Tremonti, C. A., Hickox, R. C., et al. 2014, MNRAS, 441, 3417
Setton, D. J., Bezanson, R., Suess, K. A., et al. 2020, ApJ, 905, 79
Shen, S., Mo, H. J., White, S. D. M., et al. 2003, MNRAS, 343, 978
Sijacki, D., Vogelsberger, M., Genel, S., et al. 2015, MNRAS, 452, 575
Smercina, A., Smith, J.-D. T., French, K. D., et al. 2022, ApJ, 929, 154
Spilker, J. S., Aravena, M., Phadke, K. A., et al. 2020a, ApJ, 905, 86
Spilker, J. S., Phadke, K. A., Aravena, M., et al. 2020b, ApJ, 905, 85
Straatman, C. M. S., Labbé, I., Spitler, L. R., et al. 2014, ApJL, 783, L14
Suess, K. A., Bezanson, R., Spilker, J. S., et al. 2017, ApJL, 846, L14
Suess, K. A., Kriek, M., Bezanson, R., et al. 2022, ApJ, 926, 89
Suess, K. A., Kriek, M., Price, S. H., & Barro, G. 2019a, ApJ, 877, 103
Suess, K. A., Kriek, M., Price, S. H., & Barro, G. 2019b, ApJL, 885, L22
Suess, K. A., Kriek, M., Price, S. H., & Barro, G. 2020, ApJL, 899, L26
Suess, K. A., Kriek, M., Price, S. H., & Barro, G. 2021, ApJ, 915, 87
Szomoru, D., Franx, M., & van Dokkum, P. G. 2012, ApJ, 749, 121
Tacchella, S., Dekel, A., Carollo, C. M., et al. 2016, MNRAS, 458, 242
Tacchella, S., Conroy, C., Faber, S. M., et al. 2022, ApJ, 926, 134
Takada, M., Ellis, R. S., Chiba, M., et al. 2014, PASJ, 66, R1
Tanaka, M., Valentino, F., Toft, S., et al. 2019, ApJL, 885, L34
Thorp, M. D., Ellison, S. L., Simard, L., Sánchez, S. F., & Antonio, B. 2019,
           3, 482, L55
Toft, S., Gallazzi, A., Zirm, A., et al. 2012, ApJ, 754, 3
Toft, S., Smolčić, V., Magnelli, B., et al. 2014, ApJ, 782, 68
Valentino, F., Tanaka, M., Davidzon, I., et al. 2020, ApJ, 889, 93
van der Wel, A., Bell, E. F., Häussler, B., et al. 2012, ApJS, 203, 24
van der Wel, A., Bezanson, R., D'Eugenio, F., et al. 2021, ApJS, 256, 44
van der Wel, A., Franx, M., van Dokkum, P. G., et al. 2014, ApJ, 788, 28
van der Wel, A., Noeske, K., Bezanson, R., et al. 2016, ApJS, 223, 29
van Dokkum, P. G., Nelson, E. J., Franx, M., et al. 2015, ApJ, 813, 23
van Dokkum, P. G., Whitaker, K. E., Brammer, G., et al. 2010, ApJ, 709, 1018
Wellons, S., Torrey, P., Ma, C.-P., et al. 2015, MNRAS, 449, 361
Werle, A., Poggianti, B., Moretti, A., et al. 2022, ApJ, 930, 43
Whitaker, K. E., Bezanson, R., van Dokkum, P. G., et al. 2017, ApJ,
  838, 19
Whitaker, K. E., Kriek, M., van Dokkum, P. G., et al. 2012a, ApJ, 745, 179
Whitaker, K. E., van Dokkum, P. G., Brammer, G., & Franx, M. 2012b, ApJL,
   754, L29
Wild, V., Almaini, O., Cirasuolo, M., et al. 2014, MNRAS, 440, 1880
Wild, V., Almaini, O., Dunlop, J., et al. 2016, MNRAS, 463, 832
Wild, V., Taj Aldeen, L., Carnall, A., et al. 2020, MNRAS, 494, 529
Wilkinson, A., Almaini, O., Wild, V., et al. 2021, MNRAS, 504, 4533
Wu, P.-F. 2021, ApJ, 913, 44
Wu, P.-F., van der Wel, A., Bezanson, R., et al. 2018, ApJ, 868, 37
Wu, P.-F., van der Wel, A., Bezanson, R., et al. 2020, ApJ, 888, 77
Yagi, M., & Goto, T. 2006, AJ, 131, 2050
Yano, M., Kriek, M., van der Wel, A., & Whitaker, K. E. 2016, ApJL,
  817, L21
Zabludoff, A. I., & Zaritsky, D. 1995, ApJL, 447, L21
Zabludoff, A. I., Zaritsky, D., Lin, H., et al. 1996, ApJ, 466, 104
Zheng, Y., Wild, V., Lahén, N., et al. 2020, MNRAS, 498, 1259
Zolotov, A., Dekel, A., Mandelker, N., et al. 2015, MNRAS, 450, 2327
```